Influence of nozzle exhaust angle on supersonic retro propulsion

Amrit Tarur

A thesis
submitted in partial fulfillment of the
requirements for the degree of

MASTER OF SCIENCE IN AERONAUTICS & ASTRONAUTICS

University of Washington

2023

Reading Committee:

Owen J. H. Williams, Chair

Carl Knowlen

Program Authorized to Offer Degree:
William E. Boeing Department of Aeronautics and Astronautics

University of Washington

Abstract

Influence of nozzle exhaust angle on supersonic retro propulsion

Amrit Tarur

Chair of the Supervisory Committee:
Owen J. H. Williams
Department of Aeronautics & Astronautics

Over the past few decades, humanity has been working to land astronauts on Martian soil. Several candidate technologies and ideas are being developed around the world to counter the challenges posed by the Entry Descent Landing procedure. SRP (Supersonic Retro Propulsion) is one such idea with great potential but a very limited understanding of its working. This thesis explores the sensitivity of SRP shock geometry and standoff distance to the divergence angle of the nozzle. Four divergence angles in the range between 4 deg and 16 deg were studied. When fitted against the momentum ratio parameter ($(I_e/I_\infty)^{1/2}$), the data points of the shock standoff distance acquired from different nozzles collapsed on lines with different slopes. For the highest pressure ratio case ($P_e/P_{02} = 1.7$), a difference of 8.1% in standoff distance was observed between the highest and lowest angle. A linear trend in slope variation was revealed when plotted against the cone exit angle. The variation in the numerical value of the slope, between the lowest and highest angle, was found to be 11.48% 5.5. At high thrusts, the flow also begins to become self-similar with respect to standoff distance normalized radius of curvature. This is shown with a collapse in the data points of the R/H plot. A 2" x 2" supersonic wind tunnel was also built and assembled during the duration of this research. The design requirements necessary for optimal working conditions of SRP were explored for this wind tunnel.

TABLE OF CONTENTS

Page

List of Figures iii

Nomenclature v

Chapter 1: Introduction 1
1.1 Motivation 3
1.2 Newer SRP initiatives in mid and low L/D cases 3
1.3 Goals 4

Chapter 2: Theory and Background 6
2.1 Early SRP experiments 6
2.2 Motivation for current work 14

Chapter 3: Supersonic wind tunnel 19
3.1 Overview in SSWT 19
3.2 Experimental setup for tunnel qualification and SRP testing 24
3.3 Results of initial testing 25
3.4 Conclusions 26

Chapter 4: Experimental Apparatus & Methods 30
4.1 Ludwieg Tube 30
4.2 Retro propulsive Jet 33
4.3 Schlieren system 34
4.4 Data Analysis 35

Chapter 5: Influence of nozzle exhaust angle on SRP 40
5.1 Test conditions 40
5.2 Study of unstable cases 43

5.3 Influence of nozzle cone angle on shock geometry 44

Chapter 6: Discussion and Conclusion 51

References 53

LIST OF FIGURES

Figure Number		Page
1.1	Low-L/D (a) and Mid-L/D (b) model external geometries Edquist et al[1]) .	5
2.1	Simplified sketch of SRP flow field structures for a central nozzle configuration (adapted from Finley[2])	7
2.2	Summary of scaling parameters identified by Korzun et al[3]	10
2.3	Single central configuration nozzles used by Romeo et al[4]	11
2.4	Nozzle configuration used by Gutsche et al[5]	12
2.5	Single nozzle configuration nozzles used in different studies(Adapted from Korzun et al[3])	13
2.6	Multi gas plot - Comparison of air and helium plume interference scaling with mass flow ratio at different nozzle exit Mach numbers. (Adapted from Korzun et al[3])	15
2.7	Data collapse of non-dimensional shock standoff distance when plotted against scaled momentum ratio as shown by Jennis [6]. Here results from Romeo et al [4] are shown by star markers and results from Gutsche et al [5] are shown by diamond markers	17
3.1	Overall system layout	20
3.2	Pneumatic Diagram	22
3.3	Block diagram of the Control panel	23
3.4	Picture of Control panel	23
3.5	Insert design configurations for SRP and non-SRP experiments	27
3.6	Sample picture of flow going supersonic: Shock diamonds can be seen in the image	28
3.7	Mass flow rate vs Inlet pressure	29
4.1	Sketch of the Middle section(Double Diaphragm Breach) Adapted from Yang, 2019[7]	31
4.2	x-t diagram for a Ludwieg tube with an open test section. Adapted from Wang, 1989[8]	31

4.3 Sample CAD design for 3 of 4 nozzle angles used for the study. 1/8" diameter Mach 2 nozzles for N_2 gas 33
4.4 Schlieren setup diagram adapted from [**?**] 35
4.5 Rectangular cluster(Red) shows the which segment the segmentation algorithm identifies as the nozzle 36
4.6 Nozzle tip tracking shown as pixel location vs frame, for a sample case ($\theta = 8°$ and $P_e/P_{02} = 0.5$) 37
4.7 Process flow steps from raw data abstraction to shock extraction and curve fitting 38
4.8 Plots from shock extraction algorithm. a) shows the binarized version of the mean grey-scale image and b) shows the gradient of the binarized image . . . 39

5.1 Test condition plot emphasizing the relationship between pressure ratio, momentum ratio(I_e/I_∞), and mass flow rate ratio $\dot{m}_e/\dot{m}_\infty$ (For Mach 2 condition) 42
5.2 RMS images of four angles at lowest thrust case. The color bar indicates the range of instability between 0 to 1. 43
5.3 Standoff distance with respect to divergence angle for constant thrust case($P_e/P_{02} = 1.7$). a) 4° b) 8° c) 12° d) 16°. The green marker and green line indicate bow shock for the 4° case. Yellow marker and yellow line indicate bow shock for 16° case. 45
5.4 Shock standoff distance trend as a function of momentum ratio(I_e/I_∞). Refer to Table 5.1 for symbols and colors 47
5.5 Slope vs Angle for modified I_e/I_∞. Square markers represent Λ_I. Linear fit of data. 48
5.6 Relative Percentage Difference($RPD(\%)$) as a function of $I^{1/2}$ 49
5.7 Radius of Curvature trend as a function of I 50

NOMENCLATURE

a: Speed of sound

C: Contrast of a schlieren image

C_A: Total axial force coefficient

C_D: Drag coefficient

C_T: Thrust coefficient

D: Diameter

H: Shock Standoff distance

I: Momentum

M: Mach number

m: Mass

MW: Molecular Weight

n: Refractive index

P: Pressure

q: Dynamic pressure

S: Schlieren sensitivity

R: Radius of Curvature

T: Temperature

Symbols

Λ: Slope

θ: Nozzle divergence angle

β: Ballistic coefficient

γ: Specific heat ratio

Subscripts

j: Jet

e: Jet exit plane

0: total/stagnation condition

∞: Freestream condition

2: Post bow shock

$*$: Throat condition

b: Forebody

ACKNOWLEDGMENTS

I would first like to thank Dr. Owen Williams for his continuous support and guidance at each and every step of my thesis journey. He has taught me to be meticulous and has instilled in me a great passion for the field of Aerospace engineering. Every time I faced difficulty he motivated me and showed me the brighter side. He has been a constant source of motivation for the last two years and it has been an honor to work with someone like him who is so consistent and passionate about his work. A special thanks to Elliot Jennis for being an amazing mentor during the course of this research. I am also very grateful to all my friends and family who have shown constant love and support without which I would have never made it this far.

DEDICATION

To Mom and Dad who are my pillars of support

Chapter 1

INTRODUCTION

Humans have always been keen on exploring space for a better understanding of the universe we live in. Currently, scientists and aerospace engineers around the world are invested in developing innovative applications to put human beings on Mars. This raises an important question. Why has this never happened so far? And why is it important now? So far, NASA has been able to land famous rovers starting from the Viking missions to rovers like Curiosity and Perseverance on the Martian surface, but when it comes to landing human beings there are certain mission requirements that need to be fulfilled. A crewed Mars mission would mean a larger and significantly heavier vehicle. With an increase in payload mass requirements, there is also an increase in the difficulty to control the landing parameters of the EDL (Entry Descent and Landing) vehicle. This can mathematically be expressed as the effectiveness aerodynamic drag has on decelerating a vehicle also known as the ballistic coefficient.

$$\beta = \frac{m}{C_D * A}$$

As the mass increases the drag also needs to be increased to match the ballistic coefficient. To create more drag force we employ SRP, by thrusting rockets against the flight direction.

$$C_{D,Total} = C_D + C_T$$

Due to the lack of a thick atmosphere on planets like Mars, spacecraft with high-mass payloads are likely to accelerate at a very fast rate. In these situations, supersonic parachutes are insufficient to decelerate the vehicle in the high-energy spectrum of the descent trajectory. This is where technologies like Supersonic Retropropulsion come into play.

Supersonic Retropropulsion or SRP is mainly used for space applications in which vehicles

can be landed safely and be reused for more missions without loss of resources and damage. It utilizes rocket thrusters to generate thrust in the direction opposite to descent. This thrust force adds to the drag force the body initially has to generate more resistance during the high-energy phase of flight descent. It is also more economical to use SRP as they can be reused during missions.

Recent efforts have examined entry systems relying on SRP to establish performance requirements and operating conditions for future mission applications. Over the past few years, NASA has been working on the EDL Architecture Study (EDLAS)[9] to evaluate candidate technologies to deliver human-scale vehicles (20t payloads) to the surface of Mars. NASA is currently working on low and mid lift-to-drag (L/D) vehicles that can meet these above-mentioned requirements during the hypersonic descent phase. Current conceptual designs for landing humans on the Martian surface sometimes use supersonic retropropulsion, or the initiation of retro propulsion at supersonic freestream conditions, as part of an extended powered descent phase of flight. Similar to studies in RETALT, there are also other studies like Inflatable Aerodynamic Decelerators (IAD) where research on high-mass entry systems has been conducted.The Mars Pathfinder mission, also led by NASA, was the first to use airbags for landing on Mars. While it did not employ supersonic retropropulsion directly, the mission's successful use of airbags demonstrated that alternative landing techniques could be viable for future missions.

So now that the importance of SRP in the deceleration of EDL vehicles at the high energy phase of the descent has been discussed, let us address the challenges in the development of SRP. Full-scale SRP flight tests are extremely demanding and inefficient as billions of dollars need to be spent for each test. Flow simulations could solve the issue of testing current designs but, although CFD has advanced over the years, there are still large uncertainties in the flow modeling domain and these simulations need to be validated before the design can be ready for flight. To overcome this challenge, the idea of scaling down flight conditions to a wind tunnel setup was explored. The motivation of this study is to conduct experiments that would imitate the SRP landing technology used by EDL vehicles like Falcon 9. As it is hard to

conduct fully scaled applications, we attempt to scale down the experiment to accommodate experimental testing in a laboratory setup. We try to validate this experimental procedure by matching the flow Mach numbers. This is a more efficient way to conduct experiments as it is extremely cost-effective, time-saving, and sustainable.

1.1 Motivation

Several previous researchers like Jennis[6] and Korzun[3] have worked in accumulating and developing scaling laws and parameters that would help understand features of SRP that are essential for the deceleration of EDL vehicles. For an ideal (optimally expanded) case where the retro jet nozzle has a bell-shaped exit, the flow is expected to exit perpendicular to the exit plane. But in the case of the conical nozzle, this is not true. Since the flow leaves the exit at an angle the flow characteristics such as the bow shock standoff distance and the radius of curvature were predicted to differ for each case. Conical angles are also easy to manufacture and, since the flow spreads out as it exits it, the bow shock can be assumed to have a uniform shape and there is also less shock penetration in this case. Many investigations have been conducted in the field of scaling SRP so far but none have looked into the influence of nozzle cone angle on shock geometry.

1.2 Newer SRP initiatives in mid and low L/D cases

In recent years studies in SRP have focused more on Entry, Descent, and Landing Architecture Study (EDLAS) to evaluate possible technologies that can deliver large human-scale vehicles that are required to carry 20t payload to the Martian surface. Cianciolo et al [10] addresses low and mid L/D (lift-to-drag) vehicle concepts that satisfied mission requirements outlined by Evolvable Mars Campaign (EMC). This study helps emphasize the performance difference in aerodynamic interactions for Mid-L/D and Low-L/D cases. The study summarizes approaches that were used to generate aerodynamic interference models and plans for validating CFD results provided by Edquist et al [1]. One of the major challenges as mentioned in the study is to determine if CFD predicts challenging EDL problems in a cer-

tain range. This was not an easy task as the EDL vehicles would have to be evaluated for the wind-tunnel environment and not the actual flight environment. This is because matching relevant scaling parameters from wind tunnel setup to real flight was found to be quite complex. The study also addresses some major challenges currently being faced in the field. This includes improving navigation sensors for precision landing requirements, guidance algorithms, or validating codes for surface plume interaction. This also suggests that despite gravitational and atmospheric differences, the moon could offer opportunities to run several tests that could develop technologies.

Edquist et al in his work studied newly designed NASA model designs for low and mid L/D vehicles as shown in figure 1.1. The study investigated aerodynamic interference effects due to simulated retro rocket nozzle plumes at supersonic freestream conditions.The two wind tunnel geometries were scale versions of full-scale concepts and one of the models could accommodate different nozzle characteristics that may impact aerodynamic interference behavior like bow shock area, attack angle, radial location on the heatshield, and exit-to-throat area ratio. This in turn predicted effect of the attack angle of nozzle, predicted effect of nozzle size, nozzle area ratio. The nozzle types used for these designs were conical nozzles as seen in the figure.

1.3 Goals

The goal of this thesis is to study the effects of the divergent angle of the retro jet nozzle on the stand-off distance of the SRP bow shock. Finding the dependency of flow structures on the geometric parameter would help us understand how much variation we can expect so that we can judge the differences between different experimental and simulation results. Controlling the shock standoff distance using this parameter can be beneficial as it is crucial to find an optimal distance. This is because if the bow shock is too close to the spacecraft, excess heat is generated due to friction caused by air trapped behind the shockwave. This situation is unfavorable to the astronauts inside the vehicle. Similarly, if the bow shock is too far away and does not envelop the descending vehicle in its wake, the application of SRP

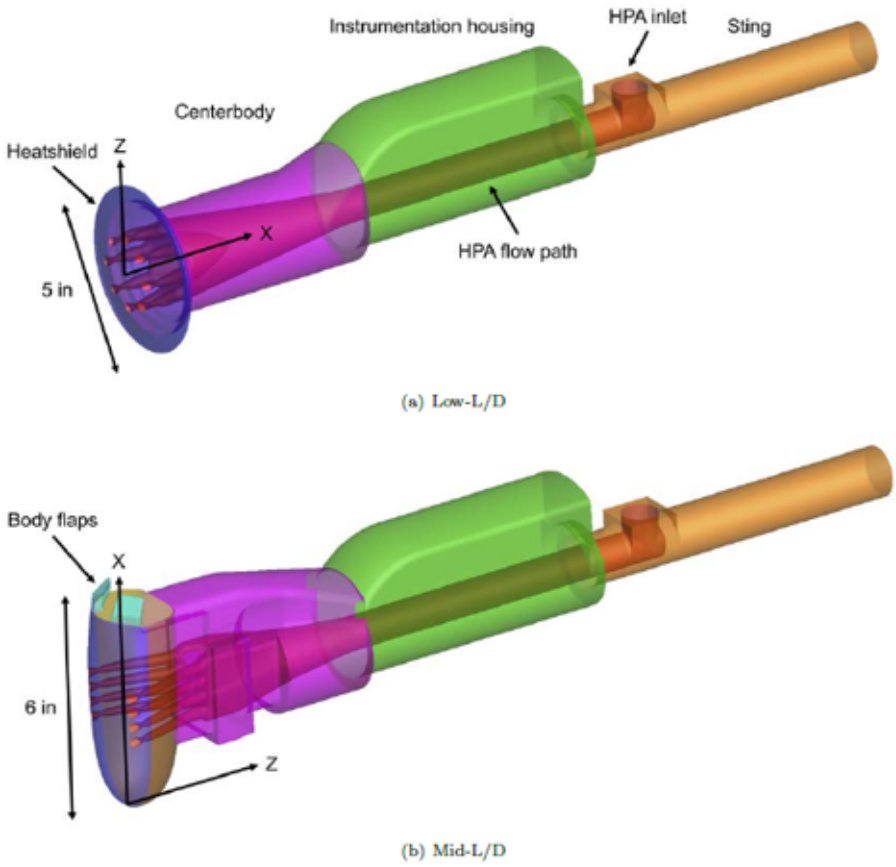

Figure 1.1: Low-L/D (a) and Mid-L/D (b) model external geometries Edquist et al[1])

could prove inefficient in decelerating the vehicle. A brief description of the experimental setup will be discussed in this work. Experiments in this study are designed in a way that the effect of the nozzle divergence angle can be recorded for different pressure ratios. To solely focus on the effect of this geometric parameter, other significant parameters including gas composition and temperatures are kept constant. Using the scaling parameter proposed by Jennis[6] the trends followed by the collected data will be assessed. Further observations made during data analysis will also be discussed.

Chapter 2

THEORY AND BACKGROUND

2.1 Early SRP experiments

Research on SRP started in the early 1960s. In 1963, Romeo and Sterrett [4] investigated the effects of a forward-facing jet on the bow shock formed before a blunt body. This was inspired by an earlier idea of injecting gas forward into the free-stream flow to see the effects of forward-facing sonic jets on the drag of a blunt body in transonic flow. Here the authors used a Mach 6 wind tunnel for a supersonic free-stream flow and five different models with varying diameters were used. High-speed schlieren photographs were used to record the flow phenomena.

Finley's [2] research contributes to a better understanding of the control parameters considered for scaled SRP experiment. In this research, the scale was assumed to be such that the variations of Reynolds number were neglected and no account of heat transfer was taken. Hence no involvement of the energy equation. Finley's experiments were conducted using a domed blunt body with a central sonic nozzle. The jet flow indicated as A shown in figure 2.1, separates and moves forward into an interface region indicated as B. A toroidal recirculation region is also formed here due to the opposing motion of the jet and free stream. This region indicated as C is also known as the Dead Air region. The fluid detached and deflected back over region C re-attaches with the blunt body surface. For Finley's experiments, a 5° conically divergent nozzle was used which was designed to produce a $M_j = 2.6$ flow. The models used by the author were hemispherical cylinders with varying diameters. The author also used single-pass schlieren and shadowgraph systems to capture and record the flow.

The region marked as "terminal shock" is also known as the Mach disc, formed when the supersonic flow that exits out of the jet turns subsonic before any interaction with the

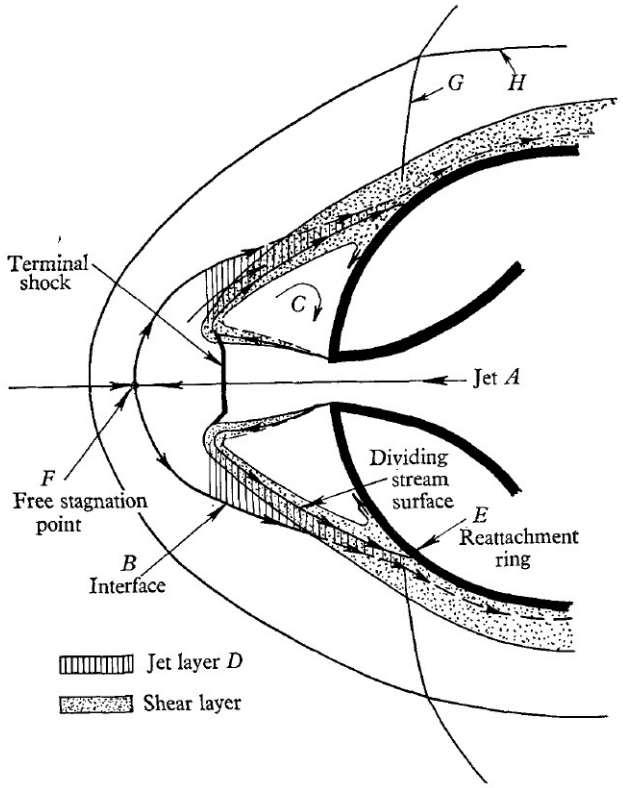

Figure 2.1: Simplified sketch of SRP flow field structures for a central nozzle configuration (adapted from Finley[2])

free stream. After crossing the terminal shock the flow slows down as it approaches the free stagnation region. At this exact point, the velocity can be observed to be almost null. It is from here that the flow separates and moves into the re-circulation region. Finley's research showed that a suitable scaling law may potentially be defined by some function of C_T, Mach number (M), and γ.

Jarvien [11] conducted SRP experiments with the goal of understanding the Aerodynamic characteristics of retro jets with large-angle conical forebodies. From the study, it was understood that at low thrusting coefficients (C_T), long jet penetration sometimes occurs whereas, at high thrusting coefficients, short blunt jet-flow interactions occur leading to the total jet head decaying with a terminal shock wave. The latter case is the major focus of

the current study. For this study, to simulate proper exhaust flow conditions the engine scaling parameter, free stream Mach number, and thrusting parameter(C_T) were matched. In addition, the expansion of jet gases and the location of the jet boundary was simulated by watching the exit pressure- free stream pressure ratio. Single nozzle 45° and 60° aeroshell models were used to conduct experiments in this study.

2.1.1 Governing variables and control parameters

Finley [2] highlights principle features and independent variables of the flow that were considered for his study in Figure 2.1. The scale for the study was assumed to be such that the variations in Reynolds number were neglected and no account is taken of heat transfer. The author defines independent variables to be those that specify the shape and size of the body and nozzle and the aerodynamic properties of both the jet and the free stream. The body shape and size are defined by fineness ($\Lambda = a/b$) and ($D = d_m/d_j$) and for thermodynamic properties of the jet and free stream, specific heat ratio was used. For dynamic similarity, the Mach numbers and total pressure ratio were used.

Pindzola [12] main focus was to study in detail the theoretical aspect of the characteristics of jets exhausting in several different scenarios. The most relevant of these cases was the moving stream case. The author also emphasizes on the importance of scaling parameters in the study of SRP. This is mainly done for convenience to perform jet tests with test fluids of different compositions and with test models of variable sizes. Thus it is pointed out that it is important to determine the scaling parameters for the results obtained for the experimental results so they can be related to that of full-scaled models. Two main relations were adapted from this study. First, for considering the mass conservation part of the problem, the ratio between the mass flow rates $\dot{m}_j/\dot{m}_\infty$ of the jet and freestream was suggested as the principle scaling parameter.

$$\frac{(\rho U A)_j}{(\rho U A)_\infty} = \frac{p_j M_j {\gamma_j}^{1/2} (RT)_\infty{}^{1/2} A_j}{p_\infty M_\infty {\gamma_\infty}^{1/2} (RT)_j{}^{1/2} A_\infty} \tag{2.1}$$

$$\left[\frac{(A_j p_j M_j)^2 \gamma_j (RT)_\infty}{(A_\infty p_\infty M_\infty)^2 \gamma_\infty (RT)_j}\right]_m = \left[\frac{(A_j p_j M_j)^2 \gamma_j (RT)_\infty}{(A_\infty p_\infty M_\infty)^2 \gamma_\infty (RT)_j}\right]_f \tag{2.2}$$

Here subscript j and ∞ refer to the retro jet and free stream properties and m and f refer to the model and full-scale conditions. In matching the conditions of the scaled setup with that of the full-scale flight condition we arrive at a relation as shown in the above equation 2.2.

Second, to consider momentum conservation, relations were developed between the model and the full-scale body. For this thrust coefficient (C_T) was introduced as it was assumed that momentum fluxes were an important factor behind the shock structure position.

$$C_F = \frac{F_j}{q_\infty A_\infty} \tag{2.3}$$

Where F_j is the thrust produced by the retro jet, q_∞ is the dynamic pressure of the free stream and A_∞ is the surface area of the free-stream exit.

$$F_j = \rho_j {U_j}^2 A_j + (p_j - p_\infty) A_j \tag{2.4}$$

Korzun et al[13] conducted a deeper analysis of Finely's [2] conceptual derivations. Using α (flow turning angle used in Finley's research) as a parameter for convergence of a finite difference method Korzun found that Finley's equations do not give a complete picture of the occurrences at the interference region even though the equations could predict Mach disc location and diameter accurately. In a later article published by Korzun et al[14], the author conducted CFD simulations on SRP flow fields and compared them with experimental results. An effort was put into finding the effectiveness of including viscous effects in capturing the actual flow physics. The study showed that viscous-turbulent solutions closely agreed with that of the experimental results when compared with viscous laminar and inviscid cases. A few years after, Korzun et al [3] brought together scaling parameters from various other studies related to SRP scaling. Scaling parameters are derived from integral equations obtained from the principles of mass, momentum, and energy. The resulting key parameters

are shown in Figure 2.2. Using mass and momentum principles two key scaling parameters were defined and these parameters will be used for the current study.

$$\Psi = \left(\frac{MW_j T_{0\infty}}{MW_\infty T_{0j}} \right)^{-1} \tag{2.5}$$

$$\Gamma = \left(\frac{\gamma_j}{\gamma_\infty} \right)^{-1} \tag{2.6}$$

Rationalizing Equations	Applications	Requirements	Scaling Parameter(s)
Navier-Stokes	All SRP geometries and flows	Continuum gases Both plume and freestream gases Smooth, solid surfaces	M_∞, Re_∞ Geometric similitude in freestream and plume flows
Momentum conservation	Approximation of the scale of AI region relative to vehicle	Meet above requirements Similar freestream and plume gas physical properties	$C_T = \frac{\tau}{q_\infty A_{ref}}$
Mass conservation	Approximation of the scale of AI region relative to vehicle	Meet above requirements Similar freestream and plume gas physical properties	$\frac{\rho_e V_e A_e}{\rho_\infty V_\infty A_\infty}$
Momentum and mass conservation	Scaling of AI flow from one set of gases to another	Meet above requirements except that for similar gas properties	γ_∞, γ_e $\frac{MW_j T_{0,\infty}}{MW_\infty T_{0,j}}$
Energy conservation	Scaling of aeroheating effects	Meet above requirements	$\frac{c_{p,j} T_{0,j}}{c_{p,\infty} T_{0,\infty}}$

Figure 2.2: Summary of scaling parameters identified by Korzun et al[3]

Korzun et al suggest two main postulates regarding the behavior of SRP flowfields: (1) Conservation of momentum-based similitude scales the size of the bow shock bounding the upstream interference region of the single nozzle supersonic retro propulsion flowfield and (2) Scaling is valid when two explicit conditions are met. The first is that the retro jet flow appears to be under-expanded and the second is that the aerodynamic thrust coefficient exceeds unity. Unfortunately, due to insufficient test results, the paper fails to test the scaling effects of various plume gas properties. The author mentions that this is due to the use of various plume gases or specific plume gas at various different chamber temperatures.

2.1.2 SRP scaling test geometries

Over the years researchers have attempted to study the effects of various forebody shapes and nozzle configurations to understand flow dependencies better.

Romeo et al[4] used five basic nozzle designs with 3 collar attachments to vary forebody sizes. Each design had a common nozzle divergence angle with varying area ratios. Although not provided, the divergence angle could be calculated using the sketch provided in the study. The total cone angle used in the study was close to 18.37°.

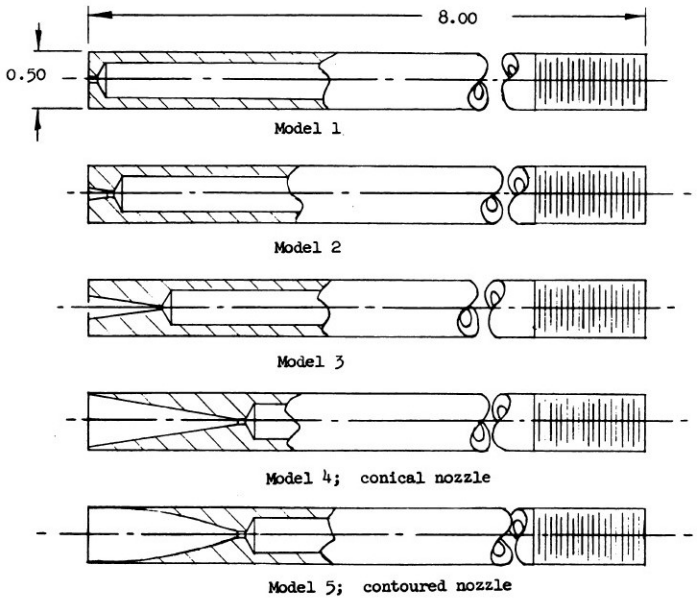

Figure 2.3: Single central configuration nozzles used by Romeo et al[4]

Gutsche et al [5] similarly used a single central nozzle to obtain results and ensure they had applicability to SRP studies. The model dimensions and test conditions were based on the RETALT1 launcher of the European RETALT project. Important modifications made to this model were model length reduction, simplification of OML, and inclusion of only one single centrally oriented nozzle. The nozzles were ideally contoured with expansion ratios of $\epsilon = 2.0$ and $\epsilon = 2.5$. The nozzle geometry is see in Figure 2.4

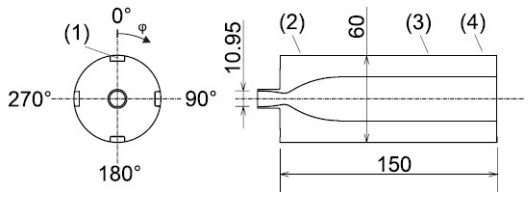

Figure 2.4: Nozzle configuration used by Gutsche et al[5]

Korzun et al [3] used axisymmetric configurations with single nozzles aligned to the center line. The configurations varied from slender blunted cylinders to blunt body aeroshells similar to the ones used in multiple previous studies. Nozzle dimensions and expansion ratios were also varied to test the dependencies of these parameters. The nozzle expansion ratio was identified using nozzle exit Mach number (M_e) and nozzle dimensions were identified using the ratio of model base diameter to nozzle throat diameter ($D_b/D*$) as defined by the author in their study. Figure 2.5 includes geometries of nozzles used in previous studies

2.1.3 Challenges in SRP development

Robert Braun et al [15] also explain concerns in some major areas of SRP development. During low thrust coefficients or high angle of attacks, the flow structures in SRP tend to become unsteady which hence leads to unstable forces and moments on the vehicle. These forces and moments can be challenging to model and cause a significant amount of uncertainty in vehicle dynamics. Effects from convective and radiative heating due to supersonic flow interaction, viscous effects, and aerothermal effects caused due to heated mixed flow including freestream and jet exhaust products enveloping the vehicle are some potential risks the author brings attention to in their study.

Even with progressing research in the field of SRP scaling, challenges arise when making assumptions and approximations during tests and drawing comparative conclusions based on those results. In general effects due to viscous forces due to shear layers in the flow interaction region, turbulence effects in the mixing region, and heating effects are complex

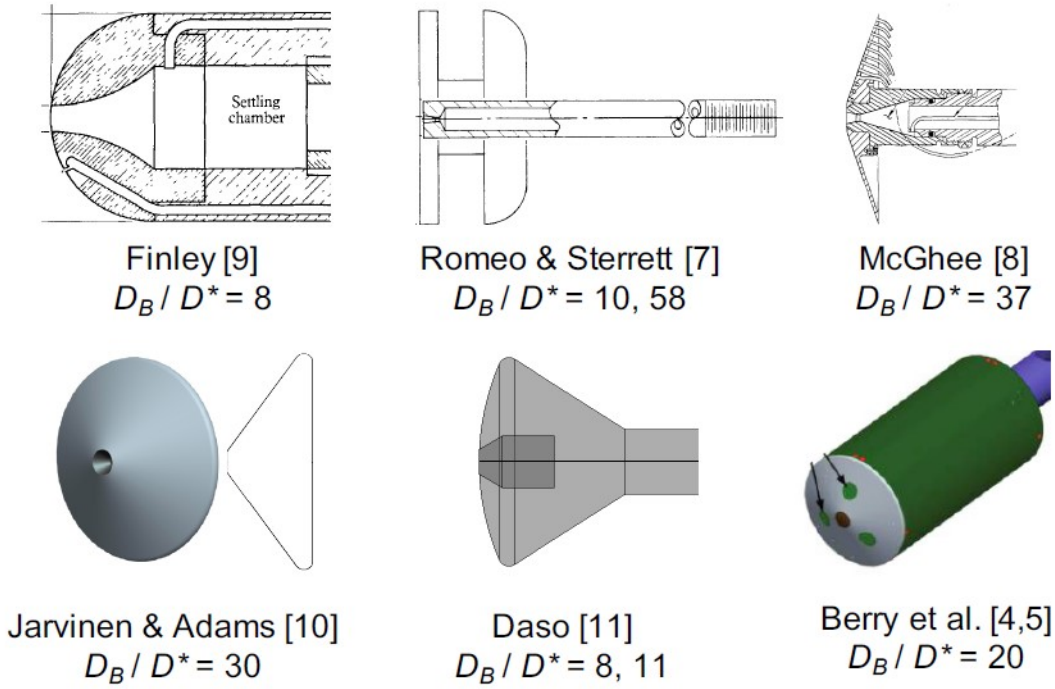

Figure 2.5: Single nozzle configuration nozzles used in different studies(Adapted from Korzun et al[3])

to study and limit the effectiveness of matching the Reynolds number as mentioned by Jennis. Korzun and Cassel also mention a discrepancy in thrust scaling while attempting to match Reynolds numbers. Over the years although multiple investigations have been conducted as the nomenclature and parameters defined are quite unique for each study, deriving a big picture has been quite a challenge.

2.2 Motivation for current work

For a supersonic nozzle, the expansion ratio is a key aspect that determines the characteristic behavior of the flow. The expansion condition is differentiated by the shape of the expanded flow egressing the exit plane. Another parameter that closely affects the appearance of the flow coming out of the nozzle exit plane in a conical nozzle is the exhaust angle.

Generally, two approaches are used for scaling rocket propulsion systems in ground testing. Either the mass flow ratio or the coefficient of thrust (C_T) between the plume and the freestream is used as they are derived from the conservation equations. Korzun and Cassel[3] address the complexity that arrives in scaling when multiple gases are involved in the flight implementation of SRP. To address this issue key scaling parameters shown in equations 2.5 and 2.6 are used.

Figure 2.6 shows the correlation of bow shock standoff distance with both the coefficient of thrust C_T and mass flow rate ratio $\dot{m}_e/\dot{m}_\infty$. Correlating shock standoff distance with p_e/p_{02} would potentially be able to express the expansion condition of the retro jet and the exact changes in standoff distance due to the shift from over-expanded to under-expanded condition. But as p_e/p_{02} is an approximation made neglecting the mixing and turbulent effects of the AI region beyond the bow shock, C_T and $\dot{m}_e/\dot{m}_\infty$ are considered as more accurate and effective as a candidate scaling parameter.

Jennis [6] focuses on the scaling of shock standoff distance with respect to two main thermodynamic parameters namely coefficient of thrust and mass flow rate ratio. The author's work also gives a brief understanding of the effects of heated and unheated SRP interactions with a variety of gas combinations. It was found that on changing the temperature of the

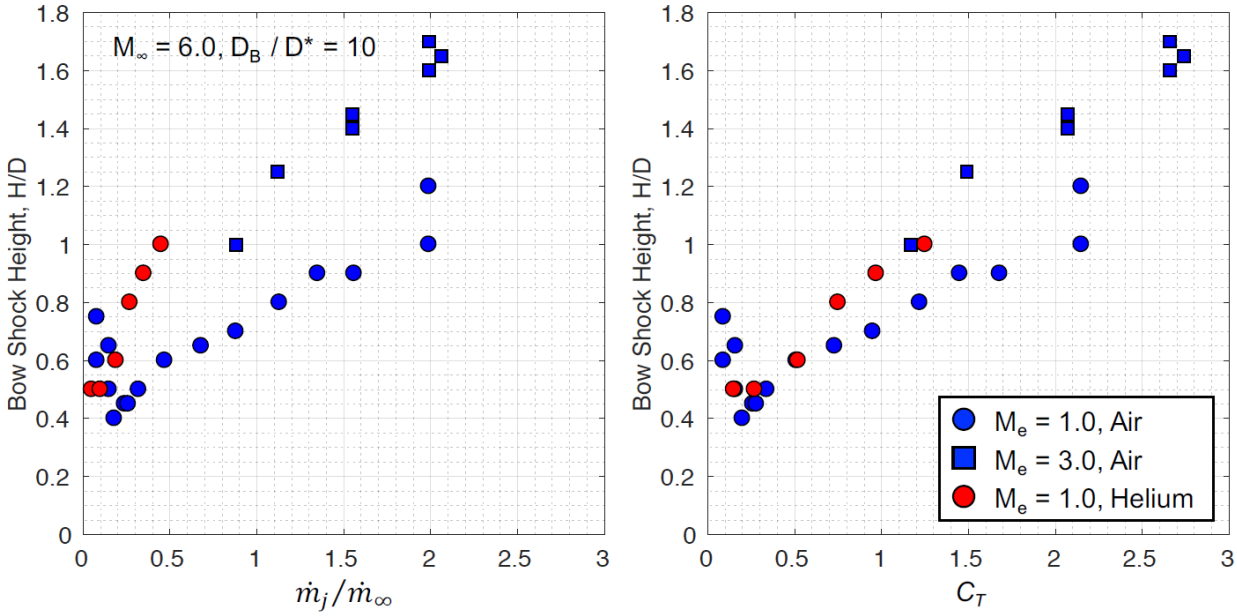

Figure 2.6: Multi gas plot - Comparison of air and helium plume interference scaling with mass flow ratio at different nozzle exit Mach numbers. (Adapted from Korzun et al[3])

gases in the system a significant difference was observable in the shock standoff distance. Similar trends were also observed for the shock radius of curvature when compared to shock standoff distance. Self-similarity in the bow shock shape was also observed regardless of the gas composition of the free stream and retro jet. Momentum ratio is shown to have collapsed shock standoff distance irrespective of the gas composition or temperature.

During an attempt to collapse shock standoff distance with the momentum ratio(I_j/I_∞), as shown in figure 2.7, Jennis[6] raised a critical question when the author observed a similarity between his study and Romeo et al [4] and a difference between these results and the results obtained by Gutsche[5]. Jennis hypothesized that Gutsche's results did not show Mach number dependency as the range of the data set was too small or maybe a different factor, such as the nozzle internal structure.

$$\frac{I_e}{I_\infty} = \frac{\rho_e * U_e^2 * A_e}{\rho_\infty * U_\infty^2 * A_b} = \frac{\dot{m}_e}{\dot{m}_\infty}\left(\frac{U_e}{U_\infty}\right)$$

$$= \frac{\dot{m}_e}{\dot{m}_\infty}\left(\frac{M_e * a_e}{M_\infty * a_\infty}\right) = \left(\frac{\dot{m}_e}{\dot{m}_\infty}\frac{M_e}{M_\infty}\right)\sqrt{\frac{\gamma_e}{\gamma_\infty}}\sqrt{\frac{MW_\infty T_e}{MW_e T_\infty}}$$

here: e = exit condition of the retro jet ∞ = freestream condition

The major difference in using I instead of C_T as a candidate scaling parameter is the use of static temperature instead of total temperature. As a result, by using the former variable we neglect the use of the pressure coefficient term in the scaling parameter.

$$\frac{I_e}{I_\infty} = C_T * \left(\frac{2}{\gamma_e * (M_e)^2} + 1\right)^{-1} \tag{2.7}$$

On further investigation, it was found that each study conducted to study scaled SRP results had varying nozzle geometry, gas combinations, and test conditions. Jennis used an 8° conical nozzle whereas Gutsche et al [5] used a contoured nozzle and Romeo et al [4] used an 18° conical nozzle. The divergence angle of a nozzle plays an important role in how flow egresses out of the exit plane. Since the divergence angle of each nozzle was different and unique it made sense to focus on testing the dependency of flow parameters on it. Korzun et

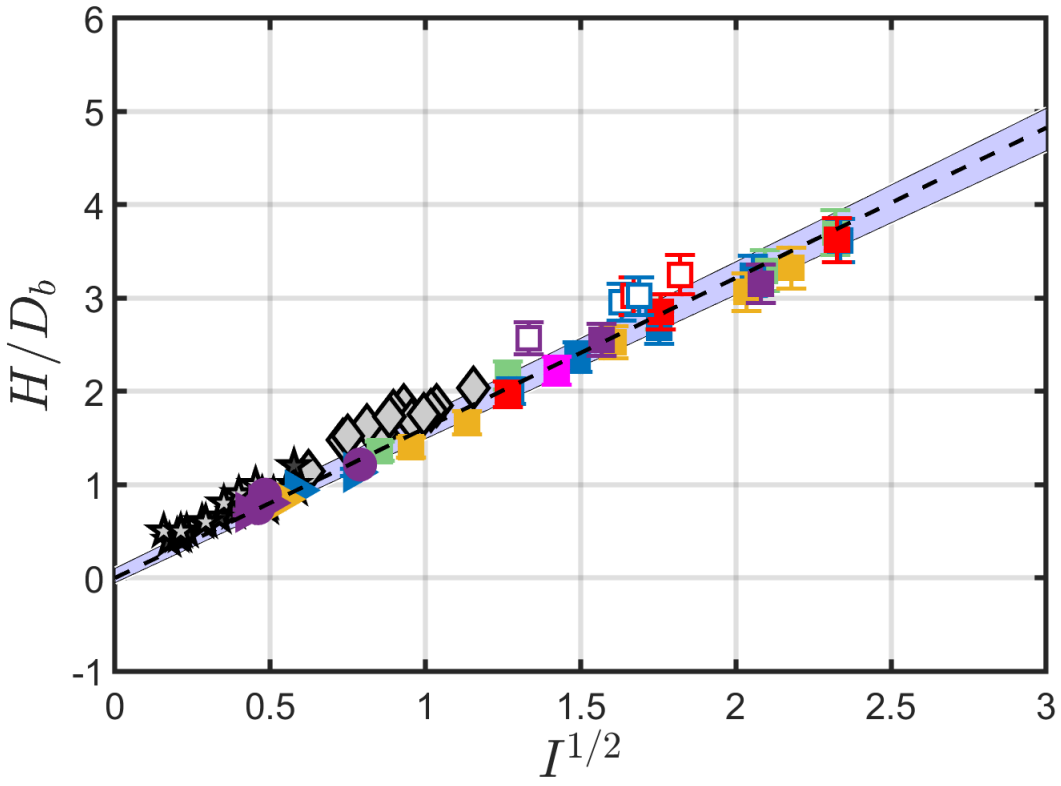

Figure 2.7: Data collapse of non-dimensional shock standoff distance when plotted against scaled momentum ratio as shown by Jennis [6]. Here results from Romeo et al [4] are shown by star markers and results from Gutsche et al [5] are shown by diamond markers

al[3] used a 15° conical nozzle for their study. Understanding the impact of this irregularity in the nozzle design used by different authors is the motivation of this study.

Chapter 3
SUPERSONIC WIND TUNNEL

Studying Supersonic Retro Propulsion requires a substantial amount of data. The primary requirement for this is to sustain free stream and retro jet flow for a significant period of time. This ensures that flow attains steady state and flow field features can be captured accurately. Currently, SRP setups in the Dept of Aeronautics and Astronautics, only capture data for a few microseconds. Due to this tests need to be conducted repeatedly to acquire data. With a supersonic wind tunnel, this repetitive process can be omitted. A pre-existing supersonic wind tunnel whose test section and nozzle were already designed and manufactured is the main subject of this section. The test section was reassembled and modified for SRP experiments.

3.1 Overview in SSWT

A supersonic wind tunnel designed to produce a flow of exit Mach number approximately between 2 to 3, was pre-designed and manufactured by the Aeronautics and Astronautics department to test supersonic flight experiments of scaled models. This chapter is separated into four segments that discuss the specifications of the SSWT individually and gives a basic understanding of the nature and workings of the wind tunnel. This chapter also addresses the architecture of the design layout and the improvements made to accommodate the needs of SRP experiments in the wind tunnel.

3.1.1 Design of the wind tunnel

The wind tunnel is a blowdown type where compressed gas, either from a compressor or a pressurized tank, is passed through two dome regulators so that the flow can be controlled,

measured, and regulated as it enters the tunnel. For this series of experiments, a compressor of outlet pressure 300psi was used. The wind tunnel has a stagnation chamber, a convergent-divergent (CD) nozzle, and a test section through which experiments can be observed. The CD nozzle has a throat area cross-section of 0.54in X 2in dimensions and an exit area cross-section of 2in X 2in dimensions. These dimensions are used in determining the inlet pressure required to operate the wind tunnel at its designated Mach number. Isentropic nozzle calculations based on nozzle design and specifications pointed out that the mass flow rate required for wind tunnel free stream nozzle to go supersonic (M 2.8) was $1.21kg/s$. The wind tunnel was separated into 7 segments as shown in Figure 3.4.

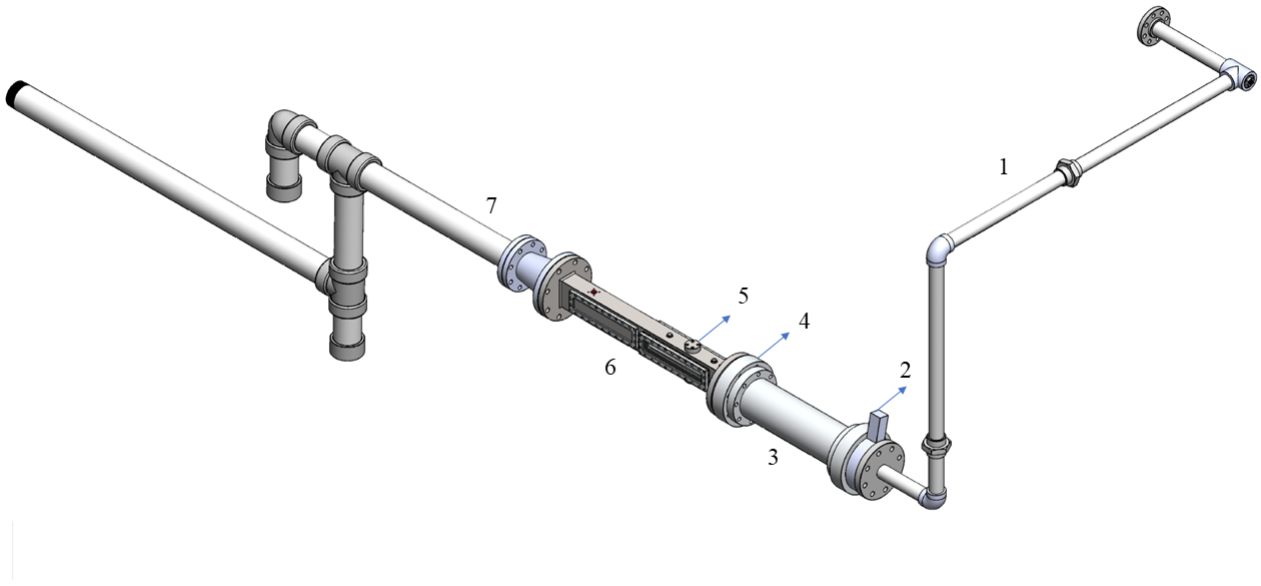

Figure 3.1: Overall system layout

Segment Number	Section Name
1	Source - Inlet
2	Main Valve
3	Stagnation Chamber
4	C-D Nozzle
5	Insert
6	Test Section
7	Exhaust

Table 3.1: Slope and constant values of the fitted line for each angle.

3.1.2 Gas supply and regulation

As discussed before there are two ways to supply air into the wind tunnel. Air is either pumped using an industrial compressor (HPCA) through the Kirsten Wind tunnel facility and then directed to the current location of the SRP lab or by using a pressurized tank stored in the facility. Using a pressurized tank would prove slightly insufficient as the mass flow rate required for the nozzle to go supersonic was calculated to be very high. This was predicted as the area cross-section of the throat and exit are considerably large. Two reducing dome regulators with a maximum inlet pressure of 3600 psi and a maximum outlet pressure of 1500 psi were utilized in the construction of the wind tunnel. The design pressures and flow rates for the regulators can be observed in the sketch shown in Figure 3.2. These regulators are essentially used to control the mass flow from the pressure source to the test section. The regulators regulate the flow by controlling the pressure difference across them. Next, a pneumatic control panel was designed to measure and regulate pressure. The control panel consists of 2 regulators each in the 0-1000 psi range. These regulators are used to control and regulate the pressure drop across each dome regulator It also consists of 3 gauges: 1) inlet pressure(from the compressor), 2) pressure at dome regulator 1, and 3) pressure at

dome regulator 2. Further study into the dome regulators uncovered that identifying the flow coefficient C_v for the specific regulator model would help obtain the mass flow rate and pressures required to operate the wind tunnel. The C_v value for model 402E regulators was found to be 12. For Gas, C_V is dependent upon upstream pressure, downstream pressure, pressure drop taken, volumetric flow rate needed, temperature, and specific gravity. The formula for C_v [16] is given by:

$$C_V = \frac{\dot{m}}{963 * \rho} * \sqrt{\frac{GT}{\Delta P(P_1 + P_2)}} \tag{3.1}$$

where: C_v = Value flow coefficient P_1 = Inlet (Upstream) Pressure, psia P_2 = Outlet (Downstream) Pressure, psia ΔP = Pressure drop, $P_1 - P_2$, psi $\dot{m}$= Mass flow rate, lb/hr G = specific gravity T = Temperature(R°)

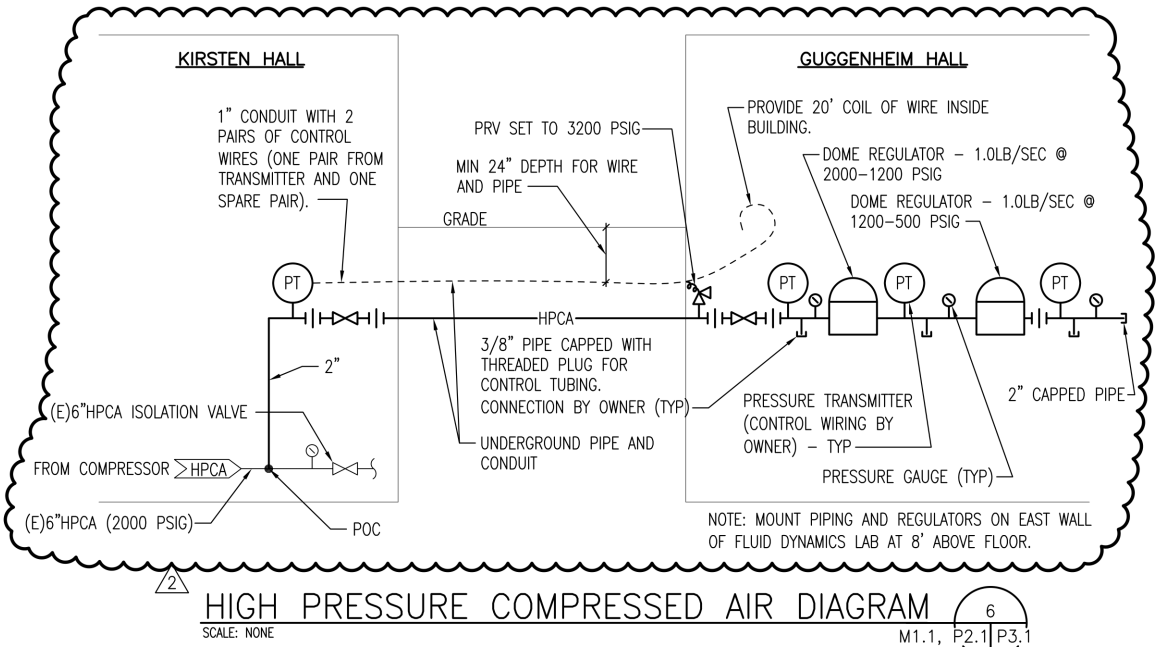

Figure 3.2: Pneumatic Diagram

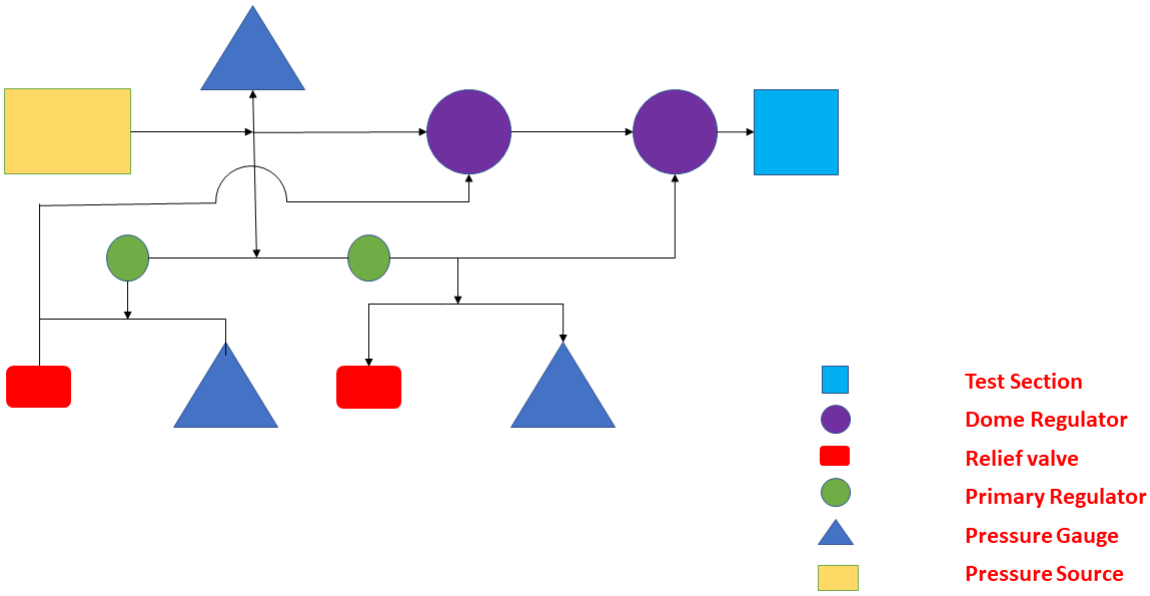

Figure 3.3: Block diagram of the Control panel

Figure 3.4: Picture of Control panel

3.1.3 Pressure and temperature instrumentation

Three pressure transducers were purchased to read the pressure measurements in the wind tunnel. Each pressure transducer has a pressure range of 0-1000 psi. Transducer 1 is placed in between two dome regulators. The 2^{nd} pressure transducer is placed in the stagnation chamber and the 3^{rd} is placed in the test section where the flow goes supersonic. This helps us keep track of the static pressures in each point so we can determine the speed of the flow and the losses occurring. A separate LabVIEW code was specifically designed by Dr. Owen Williams to extract data from the SSWT. This code is programmed to record data from 3 pressure sensors and 2 temperature sensors.

3.1.4 Test Section insert design

Two inserts were designed for the wind tunnel test section. The first configuration was designed keeping in mind that SRP experiments needed to be conducted. For this, it was important that a retro jet nozzle could be fitted and replaced as necessary, yet keeping the insert stationary. This configuration used the friction caused by yor loks for height and angle adjustment. Yor loks are plumbing fittings used to make adjustments. Since the elbow connecting to the retro jet nozzle has no other external supports, there are high chances for instability and nozzle movement during SRP experiments. For this rubber bushings can be added inside the tunnel for future experiments to ensure better stability. The second configuration was designed for flow analysis around small test specimens with various geometrical parameters. This insert is designed with a diamond-shaped wedge the design aims to cause less flow separation and hence cause as less drag as possible inside the wind tunnel.

3.2 Experimental setup for tunnel qualification and SRP testing

3.2.1 Test procedure outline

A few test experiments were conducted to validate the working of the SSWT. First tests were conducted without nozzle inserts to check if the wind tunnel achieved supersonic speeds.

After several continuous test iterations, it was brought to the conclusion that the pressure provided at the source was insufficient to carry the flow into the supersonic regime in the test section. The loss of pressure could indicate potential leaks or a lack of sufficient initial pressure from the pneumatic supply system. To identify the source of error another series of tests were conducted where pressure was allowed to build in the stagnation chamber and an impulse of airflow was provided into the test section using the main valve (segment 2) as shown in Figure 3.4. The valve had to be shut and released spontaneously in a time duration of 2-3 seconds to build this pressure before the stagnation chamber. This impulse generated enough pressure causing the flow to go supersonic for a very short amount of time. But soon as time passed the source pressure was not sufficient to keep the flow in the supersonic regime, hence the flow returns back to subsonic conditions. The tests were all conducted at ambient room temperature conditions.

3.3 Results of initial testing

The results from previously mentioned tests and conclusions derived based on these results are discussed below.

3.3.1 Mass flow requirements vs. system capability

Pressure and mass flow rate requirements did not seem to satisfy as the flow did not go supersonic in the first series of experiments. To understand better why the flow does not achieve supersonic conditions, the dome regulator specifications were used to establish a relationship between the inlet pressure and mass flow rate through the dome.

For this, the flow coefficient value C_v of a single dome regulator was used and a formula for C_v prescribed for air is used to plot the inlet pressure-mass flow rate graph.

From nozzle calculations, it was understood that the pressure required in the stagnation chamber for $M = 2.8$ supersonic flow is 117.7 psia, and the mass flow rate for choking condition at nozzle throat was calculated to be 1.23kg/s. This pressure is also known as the total charge pressure. This was set as the outlet pressure condition P_2 in the above formula.

The flow coefficient (C_v) was set to value 12 which was acquired from the design specification manual as mentioned before.

Initially, it was assumed that there was an equal pressure drop between both dome regulators. So when the inlet pressure was 300, the outlet pressure of the first dome regulator would ideally be somewhere around 200 and the outlet pressure of the second regulator was the design charge pressure (117 psia) required for the supersonic wind tunnel. When the ideal outlet pressure of the first dome regulator was the ideal inlet pressure, the required inlet pressure was found to be 315 psia, and when the ideal outlet pressure of the second dome regulator was the ideal inlet pressure, the required inlet pressure was found to be 269 psia. This can be seen in the sub-figures of figure 3.7. The outlet pressure of the first dome regulator and the inlet pressure of the second is required to match to achieve the design conditions of the supersonic wind tunnel.

3.4 Conclusions

The inlet pressure and mass flow rate requirements discussed above are for the case of each single dome regulator. From the result section it was understood that very high pressure from the source would be required to generate supersonic flow in the test section if both dome regulators are used in series. If somehow air flow either bypassed the first dome regulator or if one of the dome regulators is removed, then the exact inlet pressure that would be required can be determined from Figure 3.5b. This pressure could be achieved easier when compared with the case where two reducing dome regulators are employed.

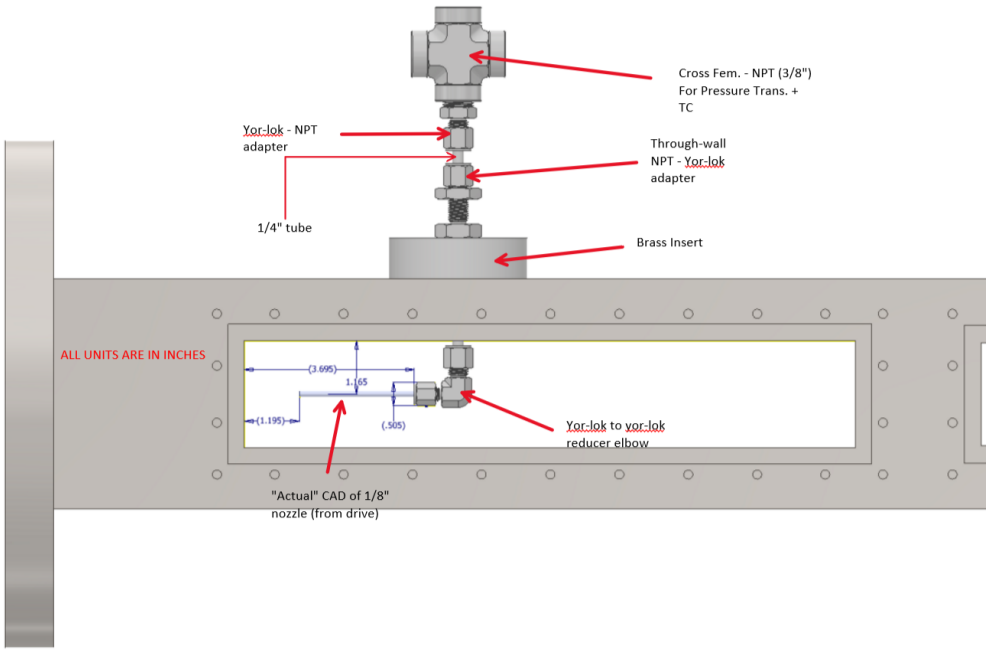

(a) Insert 1: Configuration for Retro nozzle - SRP test

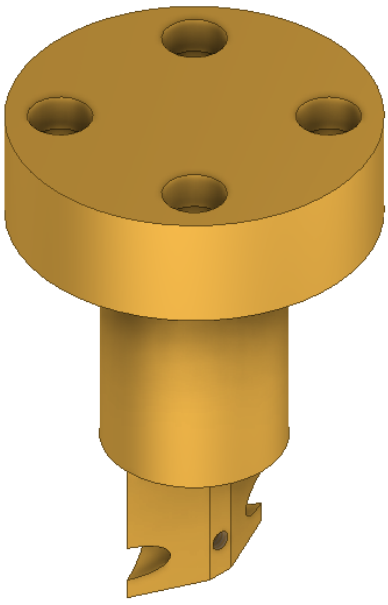

(b) Insert 2: for sharp/blunt body experiments

Figure 3.5: Insert design configurations for SRP and non-SRP experiments

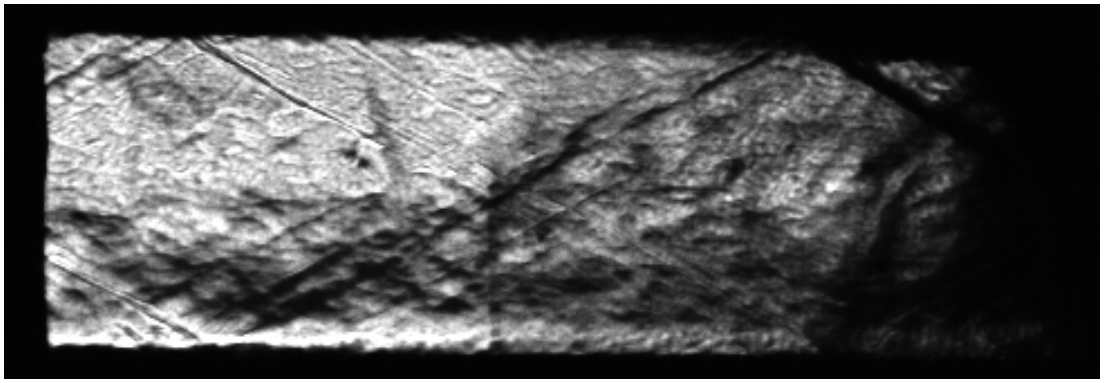

Figure 3.6: Sample picture of flow going supersonic: Shock diamonds can be seen in the image

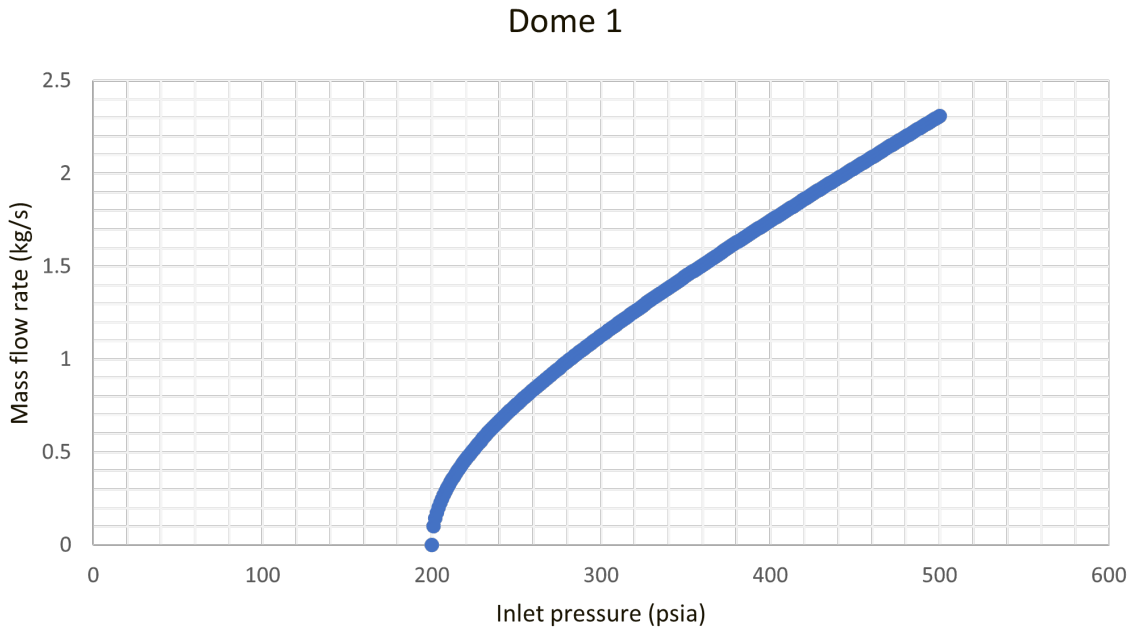

(a) Dome regulator 1

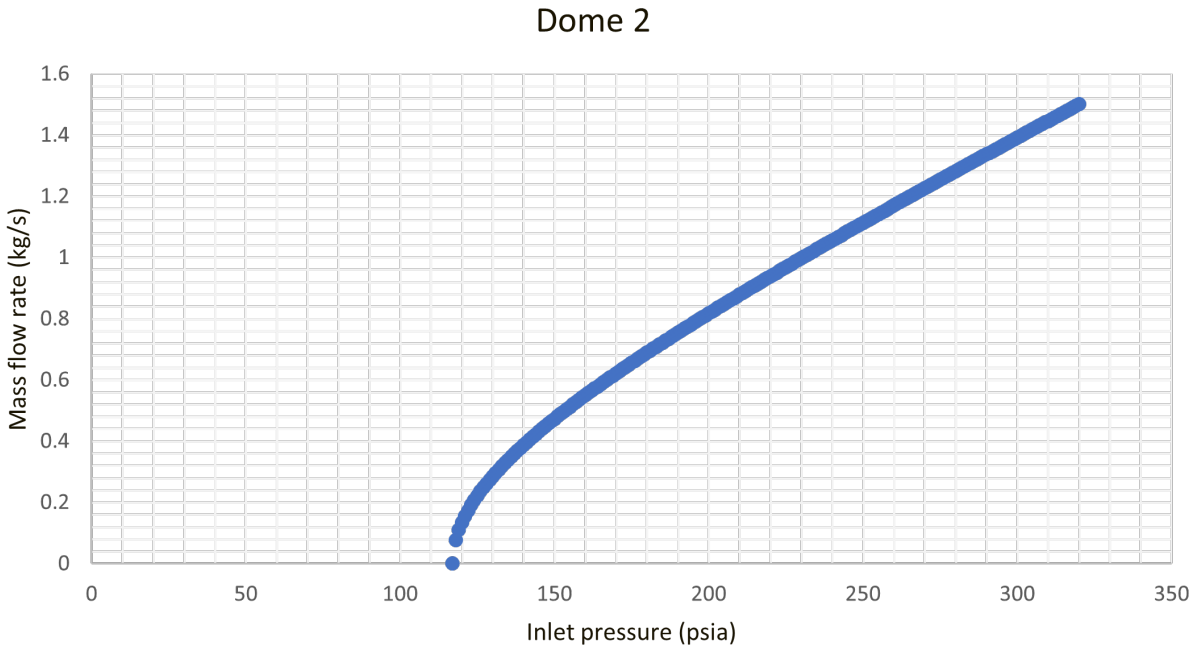

(b) Dome regulator 2

Figure 3.7: Mass flow rate vs Inlet pressure

Chapter 4

EXPERIMENTAL APPARATUS & METHODS

This chapter discusses the experimental setup, diagnostics, and analysis methods used to study SRP flowfield sensitivities to changes in nozzle exit angle.

4.1 Ludwieg Tube

To recreate scaled SRP flow conditions a free stream needs to be generated with a significant flow speed. For this reason, a ludweig tube of 3-inch diameter and 10-foot length was used in the design of this experiment. There are several ways to load a Ludweig tube and simulate the free stream flow conditions. In the case of the single diaphragm method, a single diaphragm layer is used to trigger the free stream flow. A nichrome wire is electrically charged to heat the diaphragm causing a tear in the surface. For this thesis, the double diaphragm method is used as it gives the user more controllability. In this case, the ludweig tube has 3 major sections. The first section can be understood as a stagnation chamber where pressurized air is loaded before the flow is triggered. The middle section, shown in Figure 4.1, is designed to specifically contain air to a certain pressure limit. This pressure is usually somewhere near half the charge pressure of the ludweig tube. This value for this pressure parameter was decided after several iterations where the deciding parameter was perfect flow expansion out of the nozzle. This is a function of the total charge pressure of the Ludweig tube and the thickness and material of the diaphragm. For this study, 4mm thick Mylar sheets were used as diaphragm material.

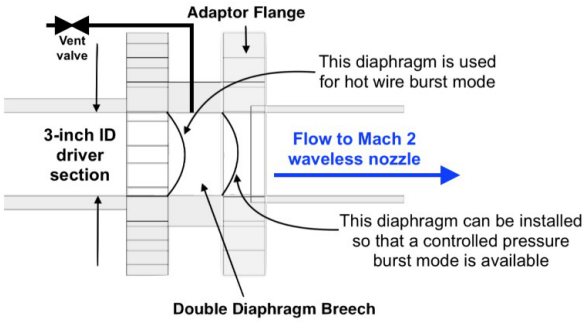

Figure 4.1: Sketch of the Middle section(Double Diaphragm Breach) Adapted from Yang, 2019[7]

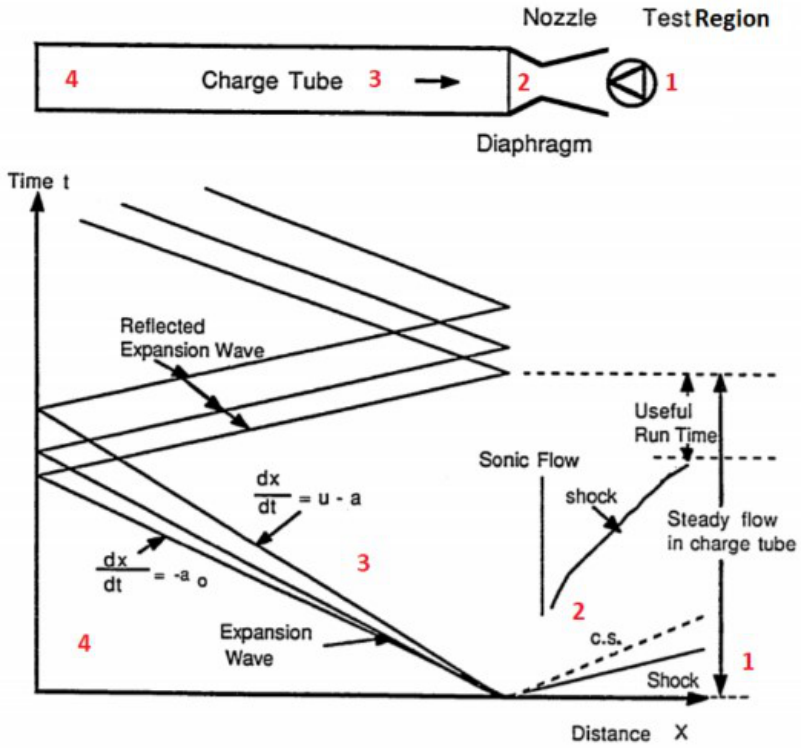

Figure 4.2: x-t diagram for a Ludwieg tube with an open test section. Adapted from Wang, 1989[8]

The final section is the nozzle section where the flow passes through the throat region and turns supersonic. Two different conical nozzles were designed based on the gas properties that were used for the experiments. CO2 ($\gamma = 1.28$) was chosen as free-stream gas and a total pressure of 110 psig is required to operate the Ludweig tube for a Mach 2 free-stream flow. The resulting configuration can produce a stable free stream for 16ms per test run.

Figure 4.2 shows the shock propagation through the ludweig tube over time after the flow has been triggered. As mentioned before, only data acquired over a short period can be analyzed as a steady case due to the change in flow properties caused by each reflection of the expansion waves.

4.2 Retro propulsive Jet

For this, a series of retro propulsive nozzles were designed and manufactured with variable nozzle exit angles. These new nozzles were based on the nozzles used by [6] and are geometrically similar.

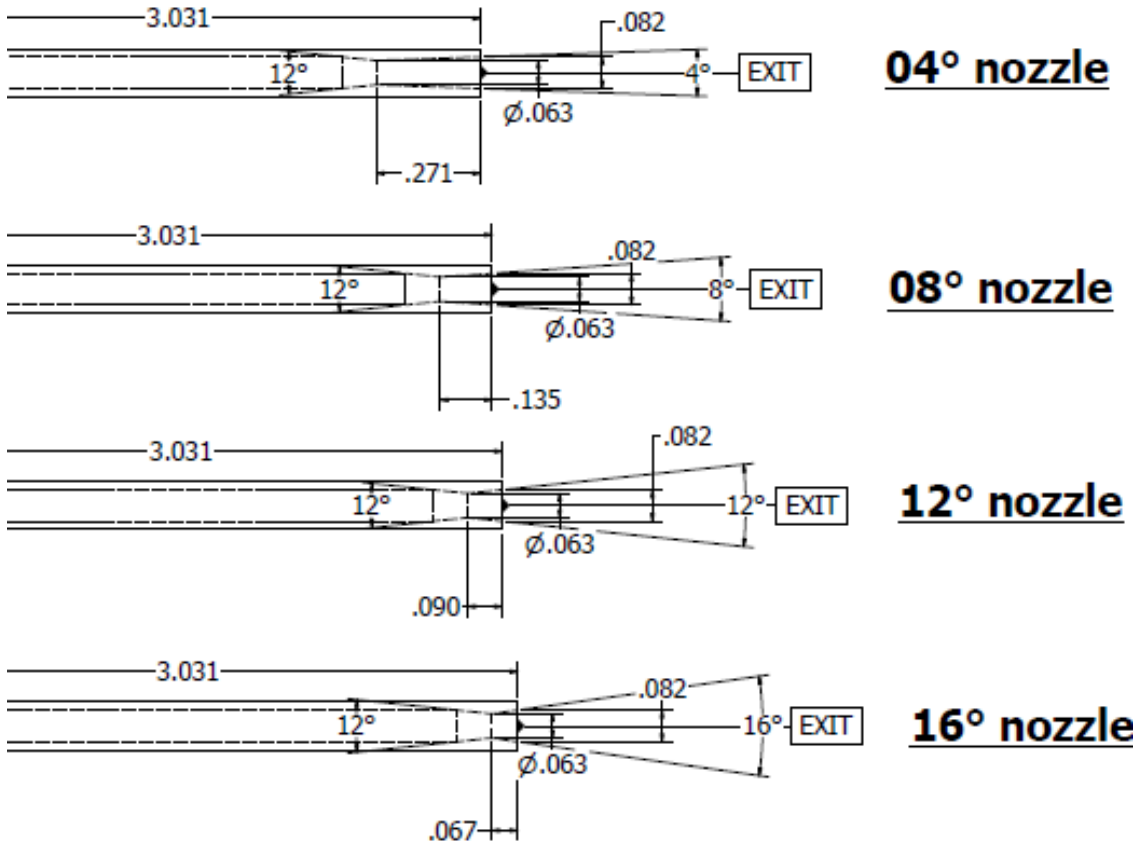

Figure 4.3: Sample CAD design for 3 of 4 nozzle angles used for the study. 1/8" diameter Mach 2 nozzles for N_2 gas

As the exhaust angle of the nozzle was the key focus of this study, four different nozzle cone angles were selected starting from 4° with increments of four. To understand only the effect of this variable all primary geometric dimensions excluding the divergence angle and

the length of the convergent-divergent section were kept constant. This includes the total length, the inlet angle, the exit area, and the forebody diameter of the nozzle. The retro jet nozzles are assumed to be isentropic and designed to produce a Mach 2 flow for diatomic gasses such as Nitrogen(N_2).

4.3 Schlieren system

Schlieren systems work on the principle of density difference observed in the flow medium. Light rays bend whenever they encounter changes in the density of a fluid medium. The system utilizes this change in density to visualize the flow and its features. Schlieren imaging works similarly to the shadowgraph technique, but the key difference is that while shadowgraphs are sensitive to changes in the second derivative in density, schlieren systems detect changes to the first derivative in density. A schlieren image differs from that of a shadowgraph with the addition of a knife-edge at the focal point of the second lens or mirror.

A phantom V 641 high-speed camera is used for collecting data in the form of a cine file. For this, the image reflected from the concave mirror is passed through a prism and focused on the center of the camera lens. the resolution of the video was set to 240 x 208. The resulting frame rate was 31,000 Hz. The camera is triggered before the flow is initiated and stopped manually after the experiment is complete. A knife edge was placed appropriately before the camera such that all the light around the focus falls into the camera. Orienting the knife in the vertical position gives gradient sensitivity in the vertical direction for the schlieren setup as shown in Figure 4.4. This design is also known as the double pass single mirror setup. The PCB assembly, designed by Yang[7], reduces the response time and smooths the incoming LED signals. The PCB also helps in better noise shielding which further improves the cleanness and responsiveness of the signals. A function generator is used to pulse the LED. Since a higher frame rate was required to capture a short time period. The pulse rate of the LED was matched with the camera's frame rate. During data analysis, an average of 370 frames per dataset was chosen for analysis. This choice was purely based on the stability of the bow shock in the recorded data. A group of frames where the position and shape of

the bow shock appeared steady were chosen for analysis.

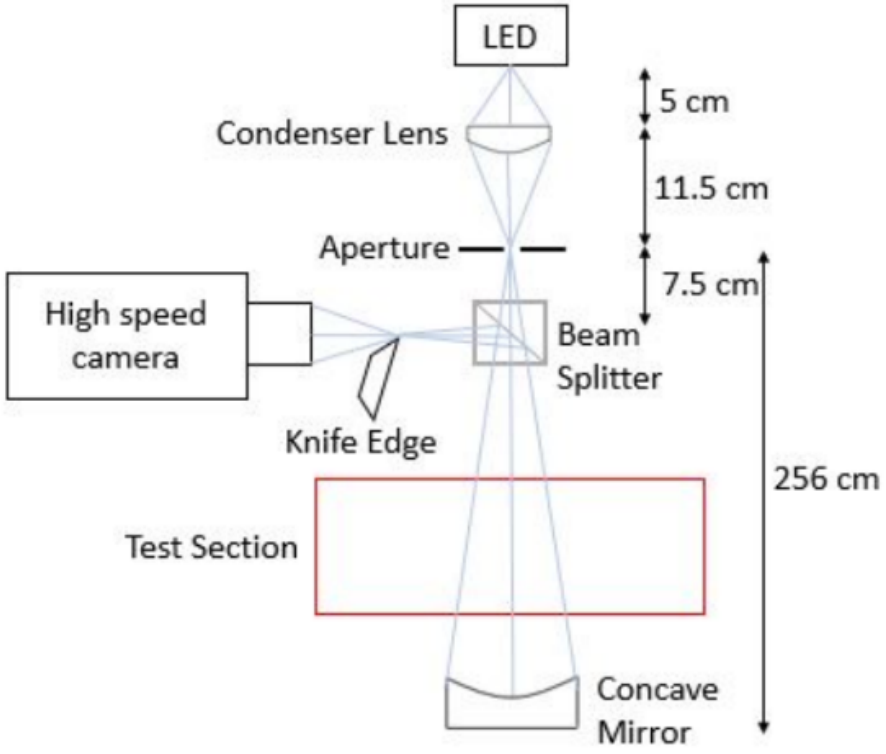

Figure 4.4: Schlieren setup diagram adapted from [**?**]

4.4 Data Analysis

After the raw data is obtained, the data is processed before the results can be extracted. The raw data is obtained as a video file in the *.cine* format. This video file can also be represented as a 3D matrix with x,y, and t coordinates respectively. A k-mean clustering algorithm [17] is used to identify the location of the nozzle in each frame. Each image is then converted into a simple black-and-white image with the red cluster representing the nozzle and the black region representing the flow field as shown in Figure 4.5. After the nozzle cluster has been identified for each frame the center point of the exit face is located. To

locate the center of the nozzle exit face, the left extreme red column of the cluster is chosen as the x coordinate and the midpoint of that column is chosen as the y coordinate hence giving us the location of the center. Locating the center point of the nozzle can tell us how the nozzle moves in the given period. Figure 4.8 shows the nozzle movement in the x and y axis with time. The nozzle tip locations were then used to stabilize the nozzle image within the frame so that it does not move.

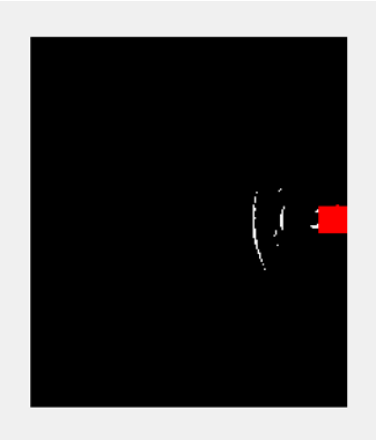

Figure 4.5: Rectangular cluster(Red) shows the which segment the segmentation algorithm identifies as the nozzle

After the locations of the centers are obtained the images for each frame are then superimposed so that the nozzles of each frame overlap one over the other. The major purpose of this segment was to eliminate disturbances caused due to shaking and vibration.

The next stage of processing is image normalization. It is important to normalize every frame by the average intensity of the frame if there is a variation in the background illumination. This is done so changes from the mean value can be clearly emphasized. The importance of normalization can be understood while extracting the mean and RMS fields. For extracting the mean field, every frame was added and averaged to display an overall picture of the nozzle location, bow shock location, terminal shock location, and internal plume structure. Similarly, the RMS field is extracted using the root mean square equation. The

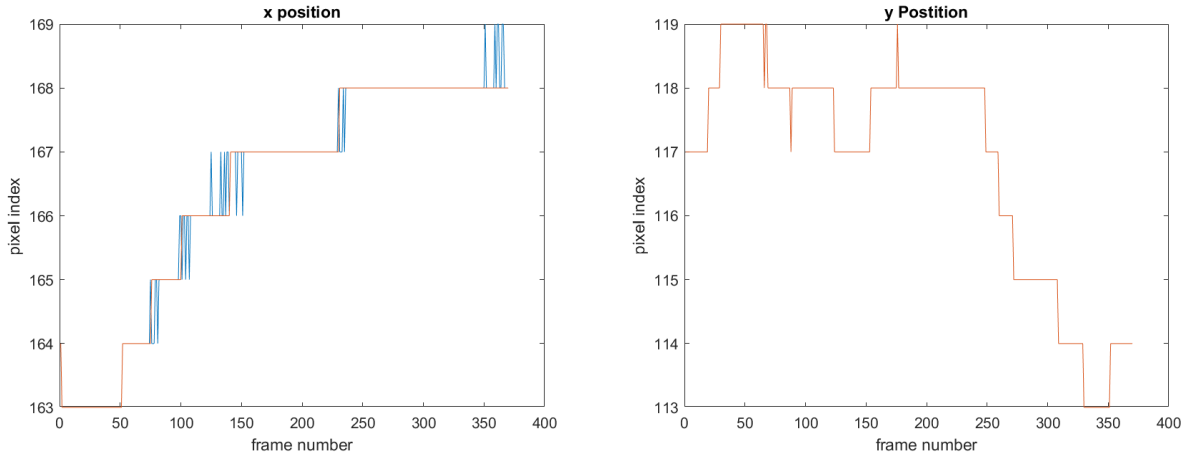

(a) x coordinate tracking

(b) y coordinate tracking

Figure 4.6: Nozzle tip tracking shown as pixel location vs frame, for a sample case ($\theta = 8°$ and $P_e/P_{02} = 0.5$)

importance of the RMS plot is to identify if the flow field is stable or unstable. Stable fields usually have less movement and hence minimal deviation from the average and unstable regions in the flow field can be identified this way. The importance of these plots will be seen further in Chapter 5.

Since unstable shocks are more complicated to study and fall under a completely different topic, this is less important in the current study. The complete flow of the processing algorithm is shown below in Figure 4.7

4.4.1 Bow shock location and radius of curvature

Once the Mean field images are obtained for a test result the goal is to isolate and distinguish the bow shock from other features in the flow field. For this, a MATLAB function *im2bw* is used. This function converts a gray-scale image into black and white when provided a certain shock prominence value. The shock prominence value can be thought of as a level. The function replaces all pixels in the input image with luminance greater than level 1

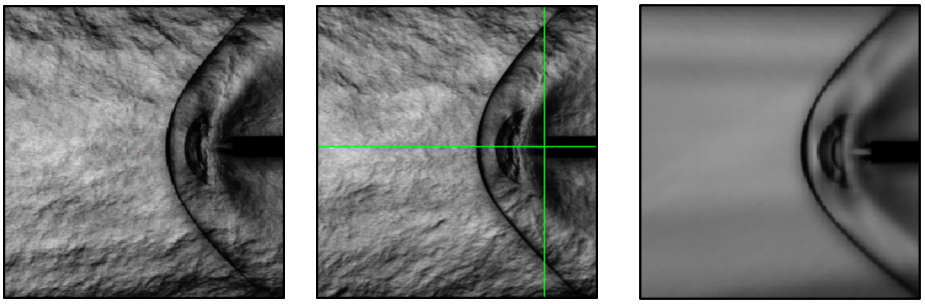

(a) Raw (b) Axes Fit (c) Mean

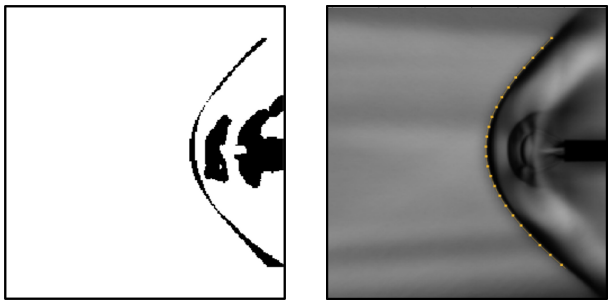

(d) Binarized (e) Shock fit

Figure 4.7: Process flow steps from raw data abstraction to shock extraction and curve fitting

(white) and all other pixels with the value 0 (black). This value is chosen by observation and iteration. Once the binarized image shown in Figure 4.8a is obtained, the image gradient is now found to detect the edge of the shock. The shock location was taken to be the first white pixel reported in each row. For this *imgradient* function with the *CentralDifference* setting selected was used.

The shock location found from the gradient image is later fitted into a curve to find the radius of curvature. For this, the poly-fit Matlab function is used to generate a polynomial function of degree 4. This approximation is made to capture the shock profile as accurately as possible. The uncertainty of the shock location is 2 pixels.

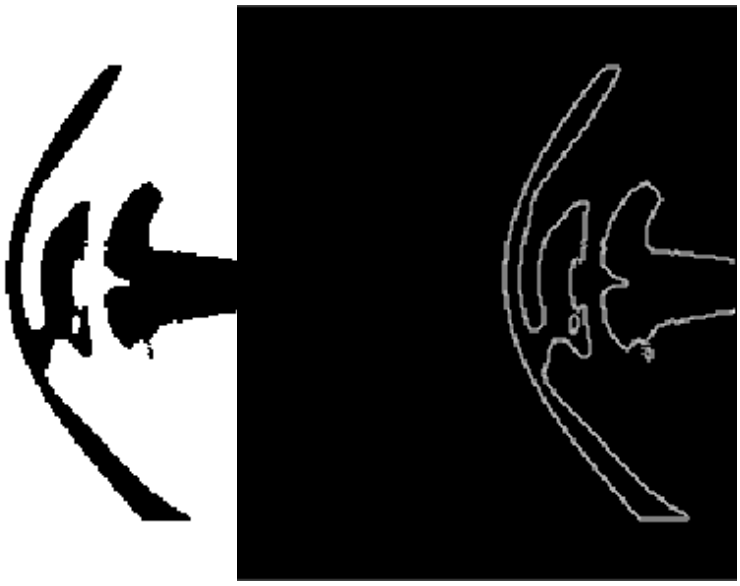

(a) Binarized Image (b) Gradient Image

Figure 4.8: Plots from shock extraction algorithm. a) shows the binarized version of the mean grey-scale image and b) shows the gradient of the binarized image

Chapter 5

INFLUENCE OF NOZZLE EXHAUST ANGLE ON SRP

5.1 Test conditions

The test conditions were chosen to test and study the exhaust angle dependency of SRP. The variables in table 5.1 are picked in such a way the experimental data set covers a wide range of pressure ratios (p_e/p_{02}). A total of five target pressure ratios are chosen, out of which two pressure ratios are chosen below one and two above one. The reason for choosing this wide pressure ratio range is to determine the trend of the nozzle angle dependency with the increase in jet pressure. For the series of experiments, as shown in the test condition matrix (Table 5.1), there was no change in the gas combination used Γ was found to have a constant value of 1.63, and since it was also understood that there is no dependency on the temperature ratio ψ is found to have a value of 1.09. After the target pressures were decided, experiments were conducted and real-time pressure values were recorded during each test. Although the same conditions were obtained for each nozzle, there was some slight variation in pressures. A summary of measured test conditions is shown in Table 5.1. In the remainder of this section symbols with filled colors indicate stable cases, and symbols with open symbols indicate the presence of instability. The occurrence of a single unstable case will be discussed in the following sections. The table also shows the range of mass flow rate ratios ($\dot{m}_e/\dot{m}_\infty$) and momentum ratios (I_e/I_∞). As the gas combination and Mach numbers are constant across all cases of the current study, it is known that the variation of shock standoff distance will be linear for both of these parameters and that both will collapse the data equally well. As a result of its more general applicability, we will focus on this parameter. The range of ($\dot{m}_e/\dot{m}_\infty$) varies between 0.72 to 3.73 while the range of (I_e/I_∞) varies between 0.91 and 4.70. For the sake of convenience (I_e/I_∞) shall from now on be referred to as I.

Test Condition and Scaling Parameters				
Symbol	θ(deg)	P_e/P_{02}	$\dot{m}_e/\dot{m}_\infty$	I_e/I_∞
■	4	0.42	0.83	1.04
	4	0.62	1.22	1.54
	4	1.13	2.23	2.83
	4	1.46	2.90	3.65
	4	1.88	3.73	4.70
■	8	0.36	0.72	0.91
	8	0.56	1.12	1.40
	8	1.16	2.31	2.91
	8	1.51	2.98	3.76
	8	1.83	3.64	4.58
■	12	0.43	0.86	1.08
	12	0.58	1.15	1.45
	12	1.05	2.08	2.62
	12	1.52	3.01	3.80
	12	1.83	3.64	4.56
■	16	0.63	1.24	1.57
	16	1.06	2.10	2.65
	16	1.55	3.05	3.86
	16	1.84	3.66	4.59
□(unstable)	16	0.42	0.83	1.04

Table 5.1: Test conditions and the resulting scaled variables found using numerical calculations

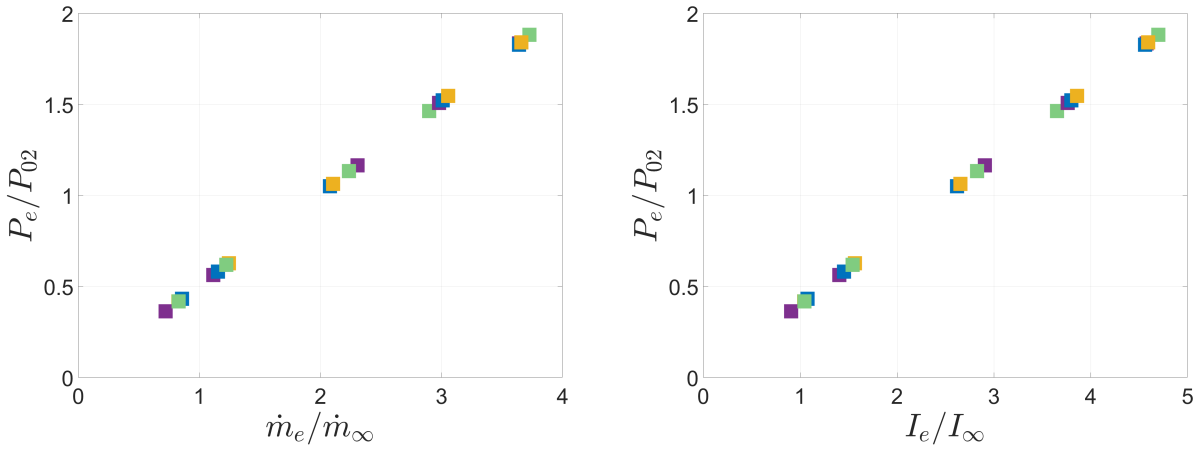

(a) (b)

Figure 5.1: Test condition plot emphasizing the relationship between pressure ratio, momentum ratio(I_e/I_∞), and mass flow rate ratio $\dot{m}_e/\dot{m}_\infty$ (For Mach 2 condition)

As seen in Figure 5.1, the points in the plot appear to align when fitted with a line. This shows that both I_e/I_{I_∞} and $\dot{m}_e/\dot{m}_\infty$ are linear functions of pressure ratio P_e/P_{02}. It is important to note that in all the cases tested, the gas properties and Mach numbers were fixed.

From Jennis [6] study, it was understood that shock geometry was more dependent on the momentum or mass flow rate ratio scaling than the pressure ratio (P_e/P_{02}). Hence, results obtained from experimental flow visualization are compared using momentum ratio (I_e/I_∞) and mass flow rate ratio $\dot{m}_e/\dot{m}_\infty$. The shock standoff distance is observed to follow a curve when plotted against C_T and mass flow rate ratio $\dot{m}_e/\dot{m}_\infty$. Jennis[6] study showed that shock standoff distance had a clear dependence on exit Mach number (M_e) and that mass flow rate ratio ($\dot{m}_e/\dot{m}_\infty$) had a clear dependence on the temperature parameter ψ, both of which are kept constant for this study.

5.2 Study of unstable cases

Previous studies pointed out that at certain low-pressure ratios, the SRP flow structures begin to show instabilities either in the form of shock oscillations or shock penetration. A similar shock instability was observed during this study when experimental cases were tested to see if stability was dependent on exhaust angle. At lower pressures for higher nozzle angles, flow separation appears to have led to flow instability. The shock instability observed during this study can be described to have a pulsating nature which closely relates to a rippling effect. Since the nature of the instability is not clear it is not defined in this study but it can be hypothesized that this kind of instability is caused due to flow separation within the nozzle due to the fact that it occurred at higher nozzle cone angles.

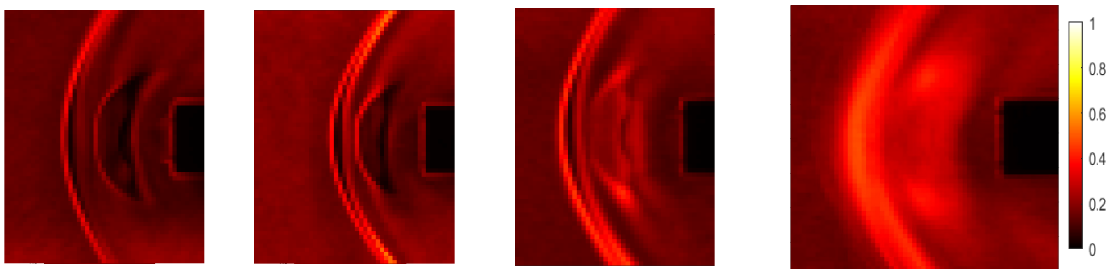

(a) $\theta = 4°$ (b) $\theta = 8°$ (c) $\theta = 12°$ (d) $\theta = 16°$

Figure 5.2: RMS images of four angles at lowest thrust case. The color bar indicates the range of instability between 0 to 1.

Figure 5.2 shows four root-mean-square images, each for one of the nozzle angles of the lowest pressure condition. The range of color-bar quantifies instability in the flowfield. Since the RMS images are normalized all pixel values fall in the range between zero and one. It is seen that as the angle value increases, the white region in the RMS plot also increases indicating a dependence on the angle parameter. Among the four cases shown only figure 5.2d was fully unstable and hence that data point had to be excluded from the study as a well-defined shock structure could not be extracted from the mean plot. A presumed

hypothesis for this behavior is explained as follows. At low pressures, as flow separates sooner in large-angle cases, the back-flow into the nozzle is greater causing a blockage at the exit for a moment. As pressure accumulates the flow is again re-attached. This cycle creates a pulsating instability that could be observed in unstable cases.

5.3 Influence of nozzle cone angle on shock geometry

A sample case was chosen to test the variation of shock standoff distance with nozzle exit cone angle. Figure 5.3 shows mean images of the four cone angles varying from 4° to 16° for the chosen sample test case. The pressure ratio ($P_e/P_{02} = 1.7$) for the sample case was chosen based on the assumption that a greater pressure ratio would show more variation in results.

The image clearly shows a variation in shock standoff distance (measured from the nozzle exit to the tip of the bow shock). The difference in the distance of the markers from the right boundary (exit face), for each of the cases proved the dependence of the shock standoff distance on the angle as discussed earlier. The magnitude of impact and the sensitivity of this variable was unknown so more tests had to be conducted to understand the flow physics. The difference in the standoff ratio for the highest and lowest angle cases is found to be 0.252. That is, the shock standoff distance(H/D_b) of the larger angle is 8.1% times greater than that of the smaller angle. Since standoff distance is normalized with forebody diameter it is clear that the difference is significant in comparison.

Figure 5.4 shows the trend nozzles of different exit angles exhibited when different pressure conditions were applied. The four lines seen in the figure are obtained by fitting steady-state data points extracted from each individual nozzle. The Y-axis quantifies the ratio of shock standoff distance to the forebody diameter. The X-axis of Figure 5.4 is simply the momentum ratio between the jet and the freestream as defined in earlier sections. The slope of the fitted lines in this study diverges with an increase in $\sqrt{I_e/I_\infty}$. This leads to an understanding that the points had to intersect at some point on the line. During the no-flow condition ($I_e/I_\infty = 0$) and ($\dot{m}_e = 0$) nozzles of the same forebody diameter must behave the same in

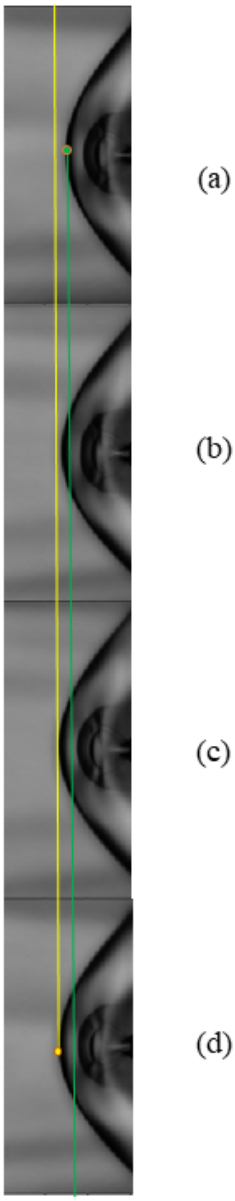

Figure 5.3: Standoff distance with respect to divergence angle for constant thrust case($P_e/P_{02} = 1.7$). a) 4° b) 8° c) 12° d) 16°. The green marker and green line indicate bow shock for the 4° case. Yellow marker and yellow line indicate bow shock for 16° case.

an SRP flow irrespective of the exhaust angle value as the bow shock standoff distance is only a function of the free stream Mach number and forebody diameter for this case. The intercept value (H/D_{b_0}) obtained from the no-flow condition of the retro jet was found to be 0.437. Considering this behavior, the lines were forced to intercept at one particular point in the y-axis. To force the intercept the polyfix[18] Matlab function was used. The linear trend (with a positive slope) hence proves the role of divergence angle in the shock standoff distance. The resulting line slopes (Λ) are expressed numerically in Table 5.2.

θ(deg)	Λ_I
4	1.23
8	1.25
12	1.32
16	1.40

Table 5.2: Slopes of the fitted lines for each angle. The intercept value at momentum ratio ($I_e/I_\infty = 0$) is 0.437

The slope of these fitted lines in Figure 5.4 are plotted against their respective angles to understand the sensitivity. The values of these slopes are given in Table 5.2. The variation of Λ vs θ is shown in Figure 5.5. Here Λ indicates the slope value of each line and θ indicates the respective exit cone angle of the nozzle. On close inspection, the square markers seem to align in a straight line exhibiting a linear trend. To understand the variation that occurs with a change in divergence angle the percentage difference was calculated using the slopes of the lowest and highest angle case. The percentage variation of the slope (Λ) across the angles is found to be 11.48%.

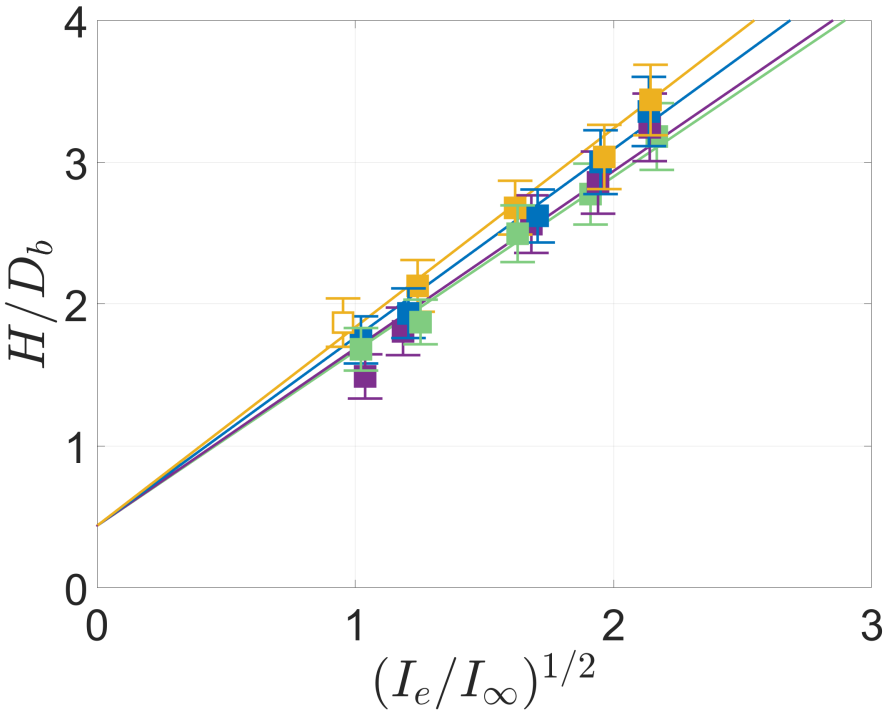

Figure 5.4: Shock standoff distance trend as a function of momentum ratio(I_e/I_∞). Refer to Table 5.1 for symbols and colors

$$\%Var = \frac{\Lambda_{16} - \Lambda_4}{\Lambda_4} * 100 \tag{5.1}$$

$$\%Var_I = 11.48 \tag{5.2}$$

For any given test conditions (thrust or mass flow) the amount of variation that is expected due to changes in the exit angle of the nozzle can be determined by calculating the Relative Percentage Difference ($RPD(\%)$). The curve seen in Figure 5.6 helps in estimating RPD of the scaling conditions with respect to the mean obtained from data points of the lowest and highest angles. For each $I^{1/2}$ case, the data point of the lowest angle is set as L and the data point of the highest angle is set as H. In this manner, $RPD\%$ is calculated using two line equations obtained from L and H. At high values of scaled moment ratio

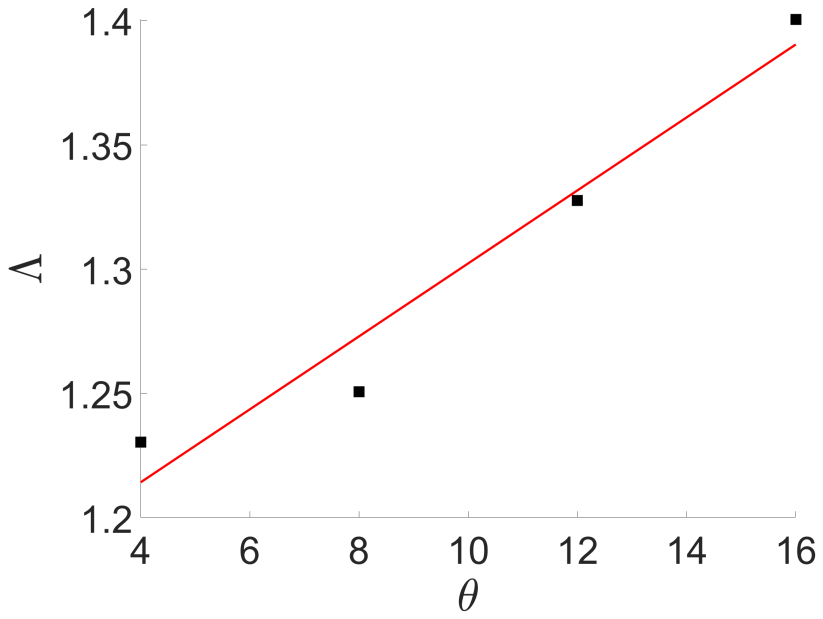

Figure 5.5: Slope vs Angle for modified I_e/I_∞. Square markers represent Λ_I. Linear fit of data.

($I^{1/2} > 50$), RPD_I approaches a limiting value of 10.84%.

$$(RPD(\%)) = \frac{H - L}{\frac{H+L}{2}} X100 \tag{5.3}$$

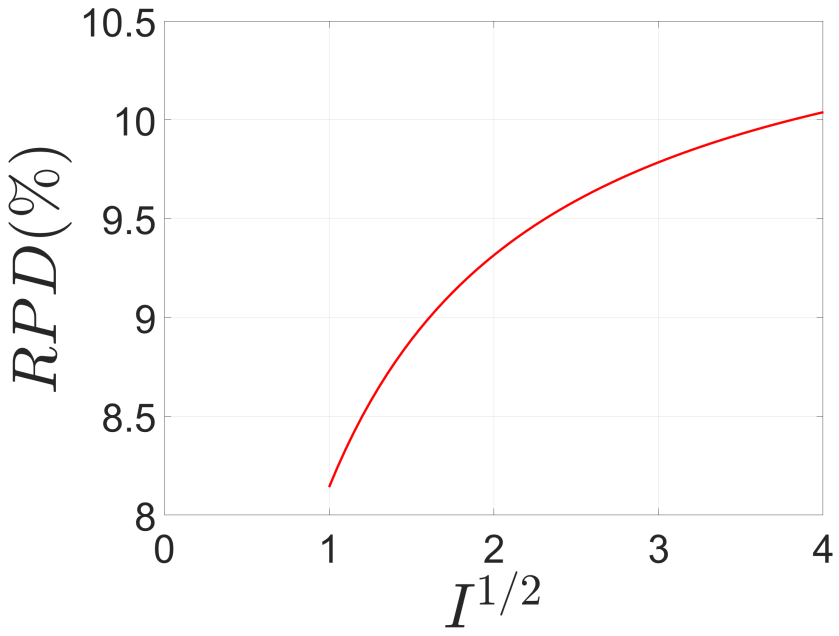

Figure 5.6: Relative Percentage Difference($RPD(\%)$) as a function of $I^{1/2}$

5.3.1 Radius of Curvature Study

Previous studies in SRP revealed that scaling laws are capable of relating thrust coefficient C_T and mass flow rate ratio ($\dot{m}_j/\dot{m}_\infty$) with the interference area enclosed by the OML (Outer Mold Line). Thus, R (Radius of Curvature) is assumed to be related to H (standoff distance) linearly. In Jennis[6], the author explained that when the radius of curvature was normalized by shock standoff distance, a small sensitivity to Mach number was potentially observed in the resulting scaling parameter (R/H). But in this study, a new geometric variable was introduced, and varying this caused a noticeable pattern to appear in (R/H) plots. As we can see in figure 5.7, the plot shows a trend where small angles have a greater R/H value for low pressures, and as the value of the divergence angle increases an inverse relationship can be observed in R/H values. This is only true for low-pressure cases and ultimately collapses at higher pressures. This could potentially prove that at high pressures

the value of the radius of curvature would be proportional to the relative shock standoff distance linearly. This could also mean that at high thrust coefficients, the flow begins to become self-similar with respect to the normalized radius of curvature parameter. Verifying this with further experimentation and analysis in the future could be an interesting study. It is also important to note here that better procedures need to be developed to estimate the error used to estimate the error in R/H calculation.

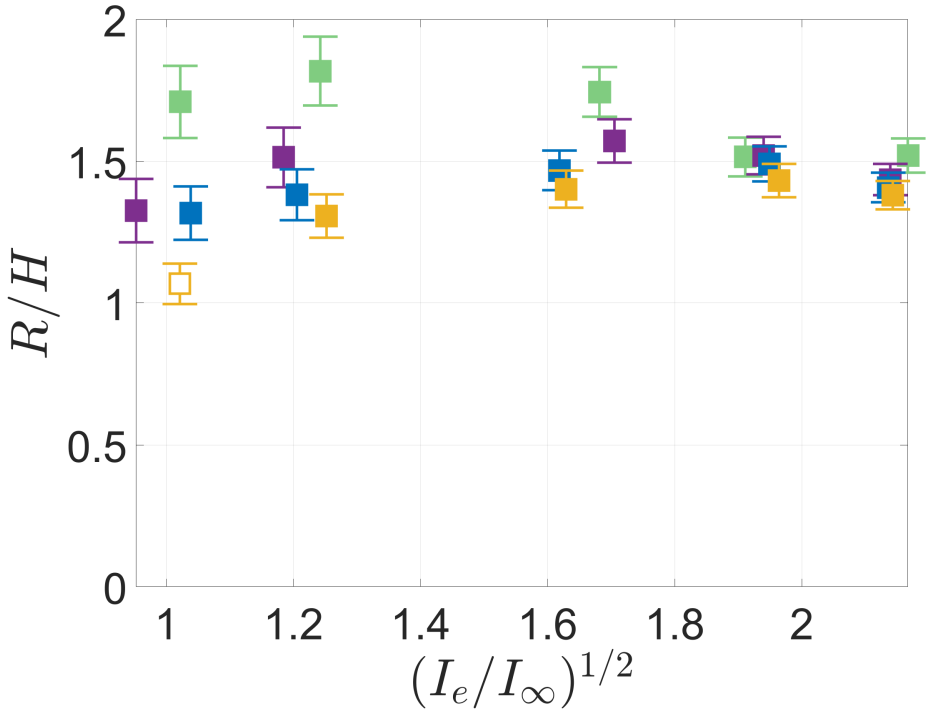

Figure 5.7: Radius of Curvature trend as a function of I

Chapter 6

DISCUSSION AND CONCLUSION

Testing the hypothesis of retro jet nozzle divergence angle dependence on shock stand-off distance helped prove the assumption of dependency in the fundamental geometric parameter. The highest pressure ratio case was selected and the bow shock standoff distance was measured for extreme angle cases 4° and 16°. The result showed an increase in shock standoff distance with an increase in the divergence angle. The shock standoff distance (H/D_b) of the larger angle is found to be 8.1% times greater than that of the smaller angle when the pressure ratio (P_e/P_{02}) is 1.7.

Bow shock standoff distance and radius of curvature were plotted against modified momentum ratio $(I_e/I_\infty)^{1/2}$ for various exit cone angles. For H/D_b, on arranging and force-fitting data points that belonged to the same angle category, a linear trend could be observed with the line intercept at the Y axis being the shock standoff distance value at no flow condition. The slopes of the lines also seemed to follow a linear trend. As the cone angle (θ) increased an increase in the slope (Λ) of the fitted was also observed meaning an increase in the shock standoff distance for a given momentum ratio case.

A plausible explanation for this behavioral pattern could be due to the difference in surface area of the interference region covered when the SRP jet impinges on it. For the same exit pressure, flow egressing from higher divergence angle nozzles is expected to cover a larger area hence applying a greater force on the bow shock. Further research with larger exit angles would need to be conducted to derive a conclusive interpretation of the sensitivity plot. The percentage variation of the slope (Λ) across the angles is found to be 11.48%.

RPD vs x-axis plots explain how much variation is expected due to changes in the exit angle of the nozzle. The interpretation is observed to become constant and converge to

one certain value after a threshold momentum ratio value of 10.84%. This indicates that at higher thrust coefficients only a fixed amount of standoff distance improvement can be gained due to changes in angle. If θ is controllable, the improvement in (H/D_b) would vary according to the initial and final angle.

The collected data set indicated instability in the highest angle case for the lowest pressure. For all other angle cases of the lowest pressure, although a steady bow shock was observed, the RMS plots indicated partial instability. A presumed hypothesis for this behavior is explained using the concept of flow separation.

Korzun and Cassel[3] postulated that scaling is valid only when two specific conditions were met. 1) P_e/P_{02} must be greater than unity and 2) C_T must be greater than unity. When these conditions are met the plume interference flowfield achieves self-similar changes in size. Standoff distance normalized radius of the curvature plots collapsed at higher I_e/I_∞ indicating self-similarity with respect to the divergence angle. Results found emphasized the importance of the radius of curvature controllability at different momentum ratios. A curious question might arise about why smaller angles have greater (R/H). For lower momentum ratio cases it is important to remember that the stand-off distance (H) which is usually smaller for small angles, hence the cumulative R/H value is greater.

For future research, CFD models can be simulated to study and verify this relationship of nozzle divergence angles with shock standoff distance. The numerical value of slope was seen to increase linearly for small angles, but this linear relationship might not be true as we go higher. Finding the threshold of this relationship and finding methods to identify and prove the cause of this behavior could also be motivation for future work.

REFERENCES

[1] Edquist, K. T., Alter, S. J., Glass, C. E., Kleb, W. L., Korzun, A. M., Wood, W. A., Canabal, F., Childs, R., Halstrom, L. D., and Matsuno, K. V., "Computational Modeling of Mars Retropropulsion Concepts in the Langley Unitary Plan Wind Tunnel," *AIAA SCITECH 2022 Forum*, 2022, p. 0912.

[2] Finley, P. J., "The flow of a jet from a body opposing a supersonic free stream," *Journal of Fluid Mechanics*, Vol. 26, No. 2, 1966, pp. 337–368.

[3] Korzun, A. M. and Cassel, L. A., "Scaling and similitude in single nozzle supersonic retropropulsion aerodynamics interference," *AIAA SciTech 2020 Forum*, 2020, p. 0039.

[4] Romeo, D. J. and Sterrett, J. R., *Exploratory investigation of the effect of a forward-facing jet on the bow shock of a blunt body in a Mach number 6 free stream*, National Aeronautics and Space Administration, 1963.

[5] Gutsche, K., Marwege, A., and Gülhan, A., "Similarity and key parameters of retropropulsion assisted deceleration in hypersonic wind tunnels," *Journal of Spacecraft and Rockets*, Vol. 58, No. 4, 2021, pp. 984–996.

[6] Jennis, E., *Thermodynamic Scaling of Supersonic Retropropulsion Flowfeilds*, Ph.D. thesis, University of Washington, 2022.

[7] Yang, X., *Influence of Jet Pressure on Multi-nozzle Supersonic Retropropulsion Flowfields*, Master's thesis, University of Washington, Arlington, Texas, May 2019.

[8] Wang, C.-M., *Transient Flow Analysis of a Supersonic Ludwieg-Tube Wind Tunnel*, Master's thesis, The University of Texas at Arlington, Arlington, Texas, May 1989.

[9] Calderon, D., Garcia, J. A., Newton, H., Amar, J., and Wiens, Z., "Human Mars entry, Descent, and Landing Architecture Study: Phase 3 Summary," *AIAA SciTech Forum*, No. JSC-E-DAA-TN76588, 2020.

[10] Cianciolo, A. D. and Polsgrove, T. T., "Human mars entry, descent, and landing architecture study overview," *AIAA SPACE 2016 Conference*, No. NF1676L-25101, 2016.

[11] Jarvinen, P. and Adams, R., "TheAerodynamicCharacteristicsof Large Angled Cones with Retrorockets," Tech. Rep. NASA-CR-124720, February 1970.

[12] Pindzola, M., "Jet simulation in ground test facilities," Tech. rep., ADVISORY GROUP FOR AERONAUTICAL RESEARCH AND DEVELOPMENT PARIS (FRANCE), 1963.

[13] Korzun, A. M., Braun, R. D., and Cruz, J. R., "Survey of Supersonic Retropropulsion Technology for Mars Entry, Descent, and Landing," *JOURNAL OF SPACECRAFT AND ROCKETS*, Vol. 46 of *5*, AIAA, American Institute of Aeronautics and Astronautics, Inc., October 2009.

[14] Korzun, A. M., Christopher E. Cordell, J., and Braun, R. D., "Comparison of Inviscid and Viscous Aerodynamic Predictions of Supersonic Retropropulsion Flowfields," Tech. Rep. 5048, Georgia Institute of Technology, Atlanta, GA, 30332, July 2010.

[15] Braun, R. D., Sforzo, B., and Campbell, C., "Advancing supersonic retropropulsion using mars-relevant flight data: An overview," *AIAA SPACE and Astronautics Forum and Exposition*, 2017, p. 5292.

[16] GE, A., "GE's Mooney Specialty Regulators - user manual search engine," 2014.

[17] Ho, B., *Characterizing Unsteadiness in Supersonic Retropropulsion Flows*, Master's thesis, University of Washington, Seattle, Washington, June 2019.

[18] Mjaavatten, A., "Polyfix, Matlab code - Used to force fit data points while curve fitting data," November 2015.

[19] Jarvine, P. O. and Adams, R. H., "TheAerodynamicCharacteristicsof Large Angled Cones with Retrorockets," Tech. Rep. CR NAS 7-576, NASA, Feb 1970.

[20] Berry, S. A. and Rhode, M. N., "Supersonic Retropropulsion Test 1853 in NASA LaRC Unitary Plan Wind Tunnel Test Section 2," Tech. rep., Langley Research Center, Hampton, Virginia, 4 2014.

[21] Korzun, A. M. and Braun, R. D., "Performance Characterization of Supersonic Retropropulsion for High-Mass Mars Entry Systems," Tech. Rep. 5, Georgia Institute of Technology, Georgia Institute of Technology, Atlanta, Georgia 30332, 2010.

[22] Berry, S. A., Rhode, M. N., Edquist, K. T., and Player, C. J., "Supersonic Retropropulsion Experimental Results from the NASA Langley Unitary Plan Wind Tunnel," 5, AIAA, American Institute of Aeronautics and Astronautics, Inc., Honolulu, Hawaii, june.

[23] Daso, E. O., Pritchett, V. E., Wang, T.-S., Ota, D. K., Blankson, I. M., and Auslender, A. H., "The Dynamics of Shock Dispersion and Interactions in Supersonic Freestreams with Counterflowing Jets," Tech. Rep. 1423, Reno, Nevada, January 2007.

[24] Fagin, M. H., *PAYLOAD MASS IMPROVEMENTS OF SUPERSONIC RETRO-PROPULSIVE FLIGHT FOR HUMAN CLASS MISSIONS TO MARS*, Master's thesis, Purdue University, West Lafayette, Indiana, December 2015.

[25] Tan, Y. M., *Influence of Pressure on Supersonic Retropropulsion Flow Field at Mach 2*, Master's thesis, University of Washington, Seattle, Washington, June 2018.

[26] Zilker, F., *Aerothermal Analysis of Re-usable First Stage during Rocket Retro-propulsion*, Master's thesis, Universität Stuttgart, Institut für Thermodynamik der Luft- und Raumfahrt (ITLR), Institute of Aerospace Thermodynamics (ITLR) Pfaffenwaldring 31, 1st floor 70569 Stuttgart, Germany, January 2018.

[27] Ecker, T., Zilker, F., Dumont, E., Karl, S., and Hannemann, K., "Aerothermal Analysis of Reusable Launcher Systems during Retro-Propulsion Reentry and Landing," May 2018.

[28] Ecker, T., Karl, S., Dumont, E., Stappert, S., and Krause, D., "A Numerical Study on the Thermal Loads During a Supersonic Rocket Retro-Propulsion Maneuver," 07 2017.

[29] Settles, G. S., *Schlieren and Shadowgraph Techniques: Visualizing Phenomena in Transparent Media*, Springer-Verlag Berlin Heidelberg, Penn State University, Gas Dynamics Laboratory, 301 D Reber Building, University Park, PA 16802, 1st ed., 2001.

[30] Lincoln, D. A., *Development and Characterization of an LED-Based Light Source for High-Speed Schlieren Imaging*, Master's thesis, University of Calgary, Calgary, Alberta, January 2016.

[31] Willert, C., Stasicki, B., Klinner, J., and Moessner, S., "Pulsed operation of high-power light emitting diodes for imaging flow velocimetry," *Measurement Science and Technology*, Vol. 21, No. 7, June 2010.

[32] Wilson, S., Gustafson, G., D. Lincoln, K. M., and Johansen, C., "Performance evaluation of an overdriven LED for high-speed schlieren imaging," *Journal of Visualization*, Vol. 18, No. 1, February 2015, pp. 35–45.